



Validation of global moderate resolution leaf area index (LAI) products over croplands in northeastern Chinas

Hongliang Fang^{a,b,*}, Yinghui Zhang^{a,b}, Shanshan Wei^{a,b}, Wenjuan Li^{a,b}, Yongchang Ye^{a,b}, Tao Sun^{a,b}, Weiwei Liu^{a,b}

^a LREIS, Institute of Geographic Sciences and Natural Resources Research, Chinese Academy of Sciences, Beijing 100101, China

^b University of Chinese Academy of Sciences, Beijing 100049, China

ARTICLE INFO

Edited by Jing M. Chen

Keywords:

Leaf area index (LAI)
Validation
Paddy rice
Global LAI products
HJ-1
Landsat
Sentinel-2A

ABSTRACT

Over the last decade, a series of global moderate resolution leaf area index (LAI) products have become available and been widely applied in many disciplines. At the same time, there is an increasing demand for the uncertainties associated with these products, which has to be determined through rigorous validation studies. This study validated seven global LAI products — EPS, GEOV2, GLASS, GLOBMAP, MODIS, PROBA-V, and VIIRS — over typical agricultural croplands in northeastern China. Seasonal continuous LAI measurements were obtained from field campaigns in paddy rice fields in 2012 and 2013, and in maize, soybean, and sorghum fields in 2016. High resolution reference LAI maps were first derived from HJ-1, Landsat 7, and Sentinel-2A images with the look-up table (LUT) inversion method and were evaluated with the field measured LAI ($R^2 = 0.85$ and $RMSE = 0.66$). Subsequently, the moderate resolution LAI products were validated with the upscaled high resolution reference LAI.

All LAI products show typical seasonal variation patterns of agricultural crops, but distinct differences exist among the products. The product quality indicators show large deviations during the peak growing season, whereas the relative uncertainties are higher during the green-up and senescent phases. Both EPS and GLASS show some saturation effects at $LAI \sim 4.0$ and underestimate the reference LAI (>0.5), whereas GLOBMAP shows the largest overestimation (bias = 0.96). GEOV2 and PROBA-V significantly overestimate the LAI for all crops. In contrast, MODIS and VIIRS underestimate and show high variations ($RMSE > 1.50$, $RRMSE > 47\%$) compared with the reference LAI. In general, the global moderate resolution LAI products show moderate agreement with the reference LAI ($RMSE: 0.80\text{--}2.0$ and $RRMSE: 25\text{--}60\%$). The product uncertainties are higher over paddy rice fields than those over the other crop fields. The uncertainties are mainly attributed to the lack of regional tuning of the global algorithms for agricultural crops at different growth stages. Further algorithm improvement and validation studies are necessary to improve the global LAI products for regional applications.

1. Introduction

Leaf area index (LAI) is one of the essential climate variables defined by the Global Climate Observing System (GCOS) for improving the parameterization of the land surface-atmosphere interaction processes in a range of models (GCOS, 2016). Over the last decade, a number of global LAI products with different spatial and temporal characteristics have become available, e.g., EPS (García-Haro et al., 2018), GEOV2 (Baret et al., 2013), GLASS (Xiao et al., 2014), GLOBMAP (Liu et al., 2013), MODIS (Huang et al., 2008; Myneni et al., 2002), PROBA-V (Baret et al., 2016), and VIIRS (Yan et al., 2018). These products have been vital in providing input to terrestrial

ecosystem and land-surface models (Fang et al., 2019).

To properly use the LAI products in various models, it is critical to understand and quantify the uncertainties associated with the products (Lafont et al., 2012; Morissette et al., 2006). The meteorological and environmental science communities have stressed the need for global and long-term validated estimates of LAI. The accuracy is expected to be a maximum of 20% or 0.5 in relative and absolute terms, respectively (GCOS, 2011). Furthermore, GCOS has updated the requirement for the relative uncertainties to a maximum of 15% (GCOS, 2016).

Many LAI products provide qualitative quality flags (QQF) and quantitative quality indicators (QQI), which contain important information about product status and uncertainties (Baret et al., 2013;

* Corresponding author at: LREIS, Institute of Geographic Sciences and Natural Resources Research, Chinese Academy of Sciences, Beijing 100101, China.
E-mail address: fanghl@lreis.ac.cn (H. Fang).

García-Haro et al., 2018; Yan et al., 2018). The QQF layer is categorical and generally describes the product processing status. The QQI layer represents the product theoretical precision caused by uncertainties in the input data, model imperfections, and the inversion process (Fang et al., 2013). The quantitative uncertainty estimates are particularly useful in data assimilation studies with land surface models (Barbu et al., 2014; Boisier et al., 2014). However, it has been noted that the theoretical precisions only represent the algorithm problems and are unable to fully represent the product uncertainties (Fang et al., 2013). Validation of the LAI products is therefore critical to evaluate whether the LAI products can meet the accuracy requirement proposed by the application community.

Direct validation of moderate resolution LAI products corresponds to the comparison of temporally and spatially concurrent satellite products with an up-scaled in situ reference LAI (Fernandes et al., 2014). Over the last decade, a number of comprehensive LAI validation studies have been performed for a variety of land cover types (Claverie et al., 2013; Fang et al., 2013; Fang et al., 2012; Garrigues et al., 2008b; Stern et al., 2014). Most of these validation studies are conducted under the framework of the Land Product Validation (LPV) subgroup of the Committee on Earth Observation Satellites (CEOS) (<http://lpvs.gsfc.nasa.gov/>). The major goal of LPV is to ensure thematic and quantitative compatibilities across products and reference datasets through commonly accepted protocols.

The goal of global validation studies is to provide product quality information for different biome types on a global scale. The global studies emphasize the global distribution and representativeness of the reference sites, but generally, do not provide an in-depth assessment of the product quality for a particular ecosystem at a regional scale (Fang et al., 2012; Garrigues et al., 2008a; Gessner et al., 2013). In parallel to the ongoing global studies, there is a need to conduct validation studies for specific ecosystem types at a regional scale. Moreover, current validation studies are usually based on a static comparison of different LAI values from different biome types. This kind of snapshot comparison would be limited for homogeneous regions with small spatial variations. In these regions, a time series validation is necessary using all LAI data obtained over the whole season (Fang et al., 2019). Nevertheless, the lack of intensive in situ measurements and satellite data have hampered the effective evaluation of existing LAI products (Garrigues et al., 2008a; Weiss et al., 2007). Only a few studies have validated the time series of moderate resolution LAI products at a regional scale (Claverie et al., 2013; Ogutu et al., 2011; Weiss et al., 2007).

The crop ecosystem is complicated because of the heterogeneity of field conditions, the diversity of crop types, the human impact (e.g. fertilizing and irrigating) on LAI dynamics, and the requirement of high temporal resolution LAI for agricultural monitoring and diagnosis. Compared to other biome types, global LAI measurements have been limited for crops (Baret et al., 2006; Fang et al., 2012). The reference data in existing studies are usually based on either a small number of sites or a local landscape, which only provide field information for a small area and a limited time (Claverie et al., 2013; Garrigues et al., 2008a). Therefore, it is critical to obtain time series of field LAI measurements for LAI product validation studies over croplands. Moreover, the time-series of LAI measurements will provide key information about the field nutrient conditions, as well as the water, energy, and carbon dynamics.

Unlike other crop types, paddy rice is grown in flooded fields; thus, the water background may affect the spectral response of the rice and the estimated LAI (Sun et al., 2017). Unfortunately, paddy rice is under-represented in the parameterization of radiative transfer models and in the training process of LAI inversion algorithms for global LAI production. In comparison to other crop types, the validation and knowledge about LAI product quality are particularly deficient for paddy rice fields (Fang et al., 2014; Urrutia, 2010). Field LAI measurements for paddy rice are, comparatively, lacking. Moreover, the uncertainties in the limited measurements available are difficult to quantify because of

the diverse environmental conditions and sampling and measurement methods employed (Fang et al., 2014). Currently, the reference LAI is mainly derived from high resolution imagery based on empirical relationships with spectral reflectance or vegetation index (Kimura et al., 2004; Shibayama et al., 2011; Vaesen et al., 2001). The empirical models are usually site-dependent and require a large amount of data to build a reliable model for validation purpose (Casanova et al., 1998; Shibayama and Akiyama, 1989).

To address the issue of inadequate ground measurements, LAI measurements were taken continuously for several growing seasons in paddy rice, maize, soybean, and sorghum fields in northeastern China (Fang et al., 2014; Fang et al., 2018). The fields are large and homogeneous, and the field data were collected following recommended guidelines with standard industry instruments. Comparisons were made between the seasonal LAI trajectories obtained by the destructive and optical measurement methods (Fang et al., 2014; Fang et al., 2018). After quality checks, the data have been made available to the public. The time series data measured in situ provide a remarkable opportunity to carry out a systematic time series validation for the global LAI products over the croplands.

The objective of the study is to validate a suite of recent LAI products derived from moderate resolution satellite data. This study provides one of the first intensive validation studies for seven LAI products — EPS, GEOV2, GLASS, GLOBMAP, MODIS, PROBA-V, and VIIRS — over croplands in northeastern China. The reference LAI maps were first retrieved from high resolution HJ-1, Landsat 7, and Sentinel-2A data using a physically based canopy reflectance model, and the results were compared with field data. The reference maps were then aggregated and compared with the moderate resolution LAI products. This study intends to address several crucial questions as follows: (1) What are the uncertainties in current LAI products as compared to high resolution reference LAI? (2) How do the current moderate resolution LAI products compare under different crop ecosystems? (3) What are the major reasons for the differences, if any, among the various LAI products and the uncertainties within the products? (4) What are the possible measures towards improving the LAI estimation for crops?

2. Study area and data

2.1. Study area and field data

Data from two sites (Honghe and Hailun) in the Heilongjiang province, northeastern China, were used in this study. The first site (centered at 47°39'N, 133°31'E) is located in paddy rice (*Oryza sativa* L.) fields in the Honghe farm (Fang et al., 2014), and the second site (47°24'–47°26'N, 126°47'–126°51'E) is planted with maize (*Zea mays* L.), soybean (*Glycine max* L.), and sorghum (*Sorghum bicolor*) in the Hailun city (Fang et al., 2018) (Fig. 1).

The Honghe site has a typical temperate humid continental monsoon climate, with a mean annual air temperature of 1.9 °C. The annual average precipitation is around 500–650 mm, with 60% of the precipitation occurring from June to September. The study site covers a total area of approximately 30 km² and has an average elevation of approximately 54 m above sea level. A single rice variety is normally transplanted in late May, and the dates for the flowering, grain filling, and maturity stages are in early-July, early August, and early September, respectively. Five plots, measuring 400 m × 600 m each, were selected in 2012 and 2013 (Table 1). Field LAI measurements were performed weekly from June 11 (day of year (DOY 163)) to September 17 (DOY 261) in 2012, and from June 22 (DOY 173) to August 27 (DOY 239) in 2013. To reduce the impact of destructive sampling and measurement disturbance, a moving sampling strategy was used (Fang et al., 2014). According to this strategy, four elementary sampling units (ESUs) within a plot were first selected for LAI measurement. The group of used ESUs was discarded in the next measurement while another four parallel ESUs were used. Approximately

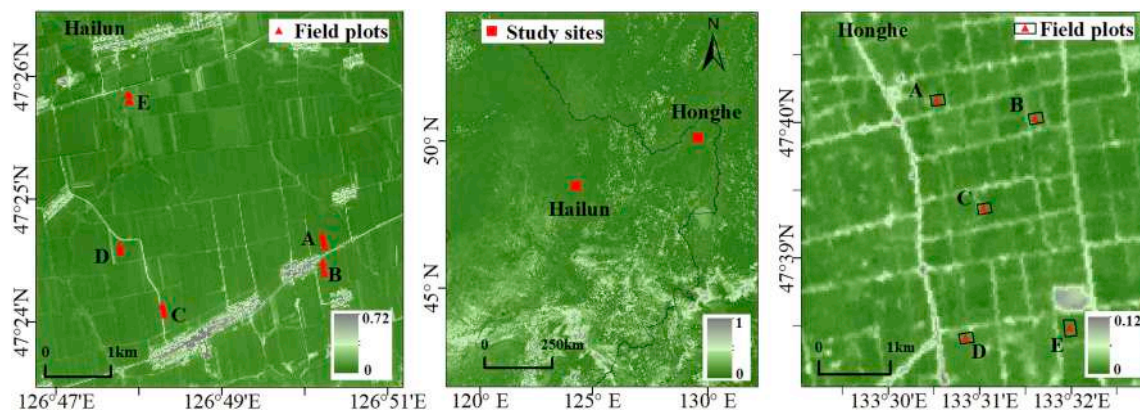


Fig. 1. Location of the study sites in Hailun (left) and Honghe (right), northeastern China (middle). The field plots are marked in red triangles. Left: Sentinel-2A MSI (665 nm, August 02, 2016); middle: MOD09A1 MODIS reflectance (620–670 nm, July 19, 2016); right: HJ-1 CCD (630 nm–690 nm, June 24, 2013). (For interpretation of the references to color in this figure legend, the reader is referred to the web version of this article.)

Table 1

Location of the plots and crop types in the Honghe and Hailun study sites for field LAI measurements with LAI-2200.

Plot	Honghe (2012, 2013)			Hailun (2016)		
	Latitude	Longitude	Crop	Latitude	Longitude	Crop
A	47.667°N	133.515°E	Rice	47.410°N	126.838°E	Maize
B	47.663°N	133.532°E	Rice	47.405°N	126.838°E	Soybean
C	47.653°N	133.523°E	Rice	47.401°N	126.805°E	Soybean
D	47.637°N	133.515°E	Rice	47.409°N	126.798°E	Maize
E	47.637°N	133.534°E	Rice	47.429°N	126.801°E	Sorghum

50 to 60 ESUs of 20 m × 20 m each were sampled within each plot. All ESU measurements within a plot measured with LAI-2200 (LI-COR Inc., Lincoln, Nebraska, USA) were averaged to represent the plot LAI (Fang et al., 2014).

The Hailun site has a similar cold temperate continental monsoon climate, with an mean annual air temperature of 2 °C. The annual average precipitation ranges from 500 mm to 600 mm, with 60–70% of the precipitation occurring from June to August. The study site has an elevation of approximately 200–240 m above sea level and covers an area of approximately 30 km². The main crops are maize, soybean, and sorghum. The maize is usually planted in early May, and the dates for tasseling, milking, and mature stages are in the end of late July, late August, and late September, respectively. The soybean and sorghum show similar growth patterns to the maize, but the soybean matures in early September (Fang et al., 2018). Five crop plots, measuring 100 m × 500 m each, were chosen for continuous LAI measurements (Table 1). Three representative ESUs of approximately 20 m × 20 m each were selected in every plot. Field LAI measurements were carried out weekly at each plot from June 20 (DOY 172) to September 22 (DOY 266) in 2016 (Fang et al., 2018).

In both Honghe and Hailun sites, field measurements were carried out during twilight and overcast conditions to avoid direct sun flecks. In both sites, the effective plant area index (PAI_{eff}) values obtained from LAI-2200 are in good agreement with the true LAI values obtained from the destructive leaf sampling method for most of the growing season from DOY 160 to 230 (Fang et al., 2014; Fang et al., 2018). Thus, the LAI-2200 measurements were considered as the true LAI values and used in the validation study.

In addition to the canopy structural measurement, field reflectance data were acquired at several homogenous sites (>60 m × 60 m in size) with an AvaField 3 spectroradiometer (Avantes, Apeldoorn, The Netherlands) over the Honghe area in June and July 2013, respectively (Table A1). The measurements were conducted between 9:00 AM and 12:00 AM local time. The radiometer was held about 1 m above the

ground surface and operated in the reflectance mode with a 25° field of view pointing at the nadir direction. Usually 50–100 sampling points were collected at each site and the average reflectance of the sampling points was used to represent the mean reflectance of the site. The measured surface reflectance data were resampled to the HJ-1 spectral bands using the spectral response functions.

2.2. Moderate resolution LAI products

Table 2 lists the moderate resolution LAI products evaluated in this study. Table 3 shows the product quality control information and the range of the values.

2.2.1. EPS LAI

The EUMESAT Polar System (EPS, V1.0) LAI is generated on a 10-day basis at the spatial resolution of 1.1 km from the AVHRR sensor onboard the Meteorological–Operational (MetOp) satellite constellation (García-Haro et al., 2018). The PROSAIL radiative transfer model (Feret et al., 2008; Verhoef and Bach, 2007) is first run to build a database of three shortwave reflectances (red, near infrared (NIR), and shortwave infrared (SWIR)) and associated biophysical parameters. A non-linear Gaussian process regression (GPR) multi-output algorithm is trained for the retrieval of LAI from the normalized spectral reflectance factor derived from a parametric bidirectional reflectance distribution function (BRDF) model. The LAI product is expressed in the range from 0 to 7. A quantitative uncertainty estimate is derived based on the theoretical model assumptions and the statistical uncertainties in the observations and the model parameters (García-Haro et al., 2018).

2.2.2. GEOV2 LAI

The GEOV2 (V2.0) LAI is derived through the Geoland2/BioPar project from the SPOT/VEGETATION (SPOT/VGT) and the PROBA-V (GEOV2/PV) observations at 1/112° and a 10-day step. When the SPOT/VGT mission ended in May 2014, the GEOV2/VGT algorithm was adapted and applied to the PROBA-V data (GEOV2/PV). The MODIS (V5) and CYCLOPES products are first combined to generate the best LAI estimates (Baret et al., 2013). A neural network training process is performed between the fused LAI and the SPOT/VEGETATION and PROBA-V daily reflectance data over the global BELMANIP sites (Baret et al., 2006). The landscape level clumping is accounted for in CYCLOPES through the separation of pure vegetation and bare soil in the pixels (Baret et al., 2007). A multi-step filtering approach, based on an iterative upper envelope process and expert knowledge on the expected seasonality, was applied to eliminate noisy data mainly affected by atmospheric effects and snow cover (Verger et al., 2014b). The quantitative uncertainties are computed using the training dataset to reflect the sensitivity of the product to the input reflectance values.

Table 2

Moderate resolution LAI products investigated in the study. LUT, NIR, NN, SWIR, SZA, and VI stand for look-up table, near-infrared, neural network method, shortwave infrared, solar zenith angle, and vegetation index, respectively.

Product ^a	Sensor	Spatial resolution	Temporal resolution	Algorithm	Period	Uncertainty provided	Reference
EPS (V1.0)	AVHRR/MetOp	1.1 km	10-day	Gaussian process regression (red, NIR, SWIR)	2015.1 +	Yes	García-Haro et al. (2018)
GEOV2 (V2.0)	VEGETATION/SPOT (1999.1–2013.12)	1/112°	10-day	NN (red, NIR, SWIR, observation geometry)	1999.1 +	Yes	Verger et al. (2014a)
GLASS (V3.1)	PROBA-V (2014 +)	500 m	8-day	NN (red, NIR)	2000 +	No	Xiao et al. (2014)
GLOBMAP (V3.0)	MODIS/Terra	500 m	8-day	Empirical VI-LAI relationship	2000 +	No	Liu et al. (2012)
MODIS (V6)	MODIS/Terra + Aqua	500 m	8-day	LUT (red, NIR)	2002.7 +	Yes	Yan et al. (2016a, 2016b)
PROBA-V (V1.0)	PROBA-V	300 m	10-day	NN (blue, red, NIR, observation geometry)	2014.1 +	Yes	Baret et al. (2016)
VIIRS (V1.0)	VIIRS/SNPP	500 m	8-day	LUT (red, NIR)	2012.1 +	Yes	Yan et al. (2018)

^a EPS (<https://landsaf.ipma.pt/en/products/vegetation/>), GEOV2 (<http://land.copernicus.eu/global/products/lai>), GLASS (<http://glass.umd.edu/> or <http://glass-product.bnu.edu.cn/>), GLOBMAP (<http://modis.cn/globalLAI/>), MODIS (<https://earthdata.nasa.gov/>), PROBA-V (<http://land.copernicus.eu/global/products/lai>), VIIRS (<https://earthdata.nasa.gov/>).

2.2.3. GLASS LAI

The Global LAnd Surface Satellite (GLASS, V3.1) LAI is estimated from the MODIS reflectance data using a general regression neural network (GRNN) approach (Xiao et al., 2014). The ‘effective’ CYCLOPES LAI (LAI_{eff}) is first converted to the true value using the clumping index (Ω) derived from the POLDER data (Chen et al., 2005):

$$LAI = LAI_{eff} / \Omega \quad (1)$$

After transformation, the MODIS and CYCLOPES LAI data are integrated in a weighted linear combination to obtain the best LAI estimate. The original MODIS reflectance data (MOD09A1) are reprocessed to remove cloud contamination, and the missing gaps are filled to obtain continuous and smooth data (Tang et al., 2013). A neural network is trained for each biome type using the combined LAI and the reprocessed MODIS reflectance data over the BELMANIP sites (Baret et al., 2006). The yearly LAI profiles are estimated using the trained GRNNs from the reprocessed MODIS reflectance data over an entire year (Xiao et al., 2014).

2.2.4. GLOBMAP LAI

The GLOBMAP (V3.0) LAI is derived by integrating the MODIS and AVHRR observations (Liu et al., 2012). The effective LAI is first generated from the MODIS land surface reflectance data (MOD09A1) based on land cover-specific LAI-vegetation index relationships simulated from a 4-scale geometrical optical model (Chen and Leblanc, 1997; Deng et al., 2006). The effective LAI is then converted to the true LAI using the 500 m global clumping index data derived from MODIS (He et al., 2012). The pixel level relationships are established between the true LAI and the vegetation indices for AVHRR and MODIS during their overlapping period. The relationships are then utilized to estimate the long term pixel level LAI for both AVHRR and MODIS over the non-

overlapping periods. The 8-day and 500 m LAI product used in this study is derived from the cloud masked MODIS reflectance data (Liu and Liu, 2013). The cloud contaminated pixels are removed by a locally adjusted cubic spline filtering approach (Chen et al., 2006).

2.2.5. MODIS LAI

The MODIS version 6 (V6) product (MCD15A2H), acquired from the combined Terra and Aqua platforms, is generated every 8 days in a 500 m spatial resolution (Myneni et al., 2015). The product is derived from a 3-D radiative transfer model using the look-up table (LUT) method (Knyazikhin et al., 1998a; Knyazikhin et al., 1998b). The mean LAI value averaged over all acceptable estimates is taken as the solution, and the standard deviation of the candidate LAI values obtained from the LUT method serves as a measure of the precision of the solution. In addition to the main LUT method, a backup algorithm is constructed based on the empirical relationship between LAI and normalized difference vegetation index (NDVI) for different biome types (Myneni et al., 1997). The V6 LAI algorithm uses the version 5 (V5) red and NIR daily surface reflectance data (MOD09GA, 500 m) and the multi-year land cover product (MCD12Q1, 500 m) (Yan et al., 2016a; Yan et al., 2016b). Companion LAI products have also been derived separately from the MODIS sensors onboard the Terra (MOD15A2H, 8-day) and Aqua (MYD15A2H, 8-day) platforms every 8 days, and also from the two platforms jointly every 4 days (MCD15A3H).

2.2.6. PROBA-V LAI

The PROBA-V (V1.0) LAI is distributed with a 10-day temporal sampling and 300 m spatial resolution through the Global Land Service of the European Commission's Copernicus program. The neural networks are trained from the best LAI estimates obtained by fusing and

Table 3

Quality control measures in processing the LAI products. QQFs: qualitative quality flags, QQIs: quantitative quality indicators.

Product	Data format	QQFs	QQIs	Quality control ^a	Usage in the study
EPS	HDF	LAI_QF	LAI_err	QQF = (0)	“No suspect” values only
GEOV2	NetCDF	LAI-QFLAG	RMSE	LAI = 0–210	Valid retrieval between 0 and 7
GLASS	HDF	Unspecified		LAI = 0–1000	Valid retrieval between 0 and 10
GLOBMAP	HDF	Unspecified			All retrievals
MODIS	HDF	FparLAI_QC	LaiStdDev	QQF = (000, 001)	Main retrievals
PROBA-V	NetCDF	QFLAG	RMSE	LAI = 0–210	Valid retrieval between 0 and 7
VIIRS	HDF	FparLAI_QC	LaiStdDev	QQF = (000, 001)	Main retrievals

^a Numbers in the brackets indicate the bit combinations of QQF.

scaling the MODIS V5 and the CYCLOPES V3.1 products (Baret et al., 2016). Different from the method employed in GEOV2, a non-linear weighting function is used to fuse the MODIS and CYCLOPES LAI products. The trained neural network is applied to retrieve the LAI from the top of aerosol PROBA-V reflectance data. The instantaneous LAI estimates are temporally smoothed and composited to generate the 10-day product. The quality control strategy employed in PROBA-V is similar to that in GEOV2.

2.2.7. VIIRS LAI

The VIIRS sensor is onboard the Suomi National Polar-orbiting Partnership (SNPP) satellite, which is an interim satellite between the Earth Observation System (EOS) and the Joint Polar Satellite System (JPSS) satellites. The VIIRS algorithm is inherited from the MODIS, but with VIIRS-specific parametrization (Yan et al., 2018). Similar to the MODIS, the VIIRS LAI (V1.0) is generated every 8 days in 500 m resolution, with the goal to develop a continuous and consistent Earth System Data Records (ESDRs). The VIIRS quality layer is also similar to that of the MODIS. Preliminary comparison of VIIRS and MODIS has shown that the two products are generally consistent (Yan et al., 2018).

2.3. High resolution remote sensing data

Three types of high resolution images were used in order to obtain sufficient number of time series data to match with the moderate resolution LAI products. Twelve cloud free HJ-1 images were obtained over the growing seasons in 2012 and 2013 at the Honghe site (Table 4). Additionally, seven cloud free HJ-1 images were obtained in 2016 at the Hailun site. The HJ-1A and HJ-1B satellites were launched on September 6, 2008. Both satellites contain a Wide View CCD (WVC) camera, which collects data in four bands from 430 to 900 nm with a 30 m spatial resolution and a repeat cycle of 4 days. The data are available from the China Centre for Resources Satellite Data and Application (CRESDA, <http://218.247.138.119:7777/DSSPlatform/index.html>).

(<http://218.247.138.119:7777/DSSPlatform/index.html>).

Two clear Landsat 7 ETM+ imagery (path 118/row 27) dated on August 13 and August 29, 2016 were downloaded from the United States Geological Survey (USGS) EarthExplorer (<https://earthexplorer.usgs.gov/>). The ETM+ data (30 m) had been corrected for atmospheric effects using the Landsat Surface Reflectance Code (LaSRC) that includes an image based spatially explicit aerosol retrieval (Vermote et al., 2016).

Two cloud free Sentinel-2A multi-spectral instrument (MSI) Level-1C (MSIL1C) images (tile 51T-YN) on August 2 and September 18, 2016 were downloaded from the Copernicus Open Access Hub (<https://scihub.copernicus.eu/>). The MSIL1C imagery have been ortho-rectified and geo-registered with sub-pixel accuracy. The Sen2Cor atmospheric correction software (Version 2.5.5) (Müller-Wilm, 2018) was used to convert the MSI data to surface reflectance. The MSI 10-m red band was resampled to match the 20 m NIR band using the nearest neighbor resampling method in the Sentinel Application Platform (SNAP 6.0, <http://step.esa.int/main/toolboxes/snap/>). For both ETM+ and MSI sensors, the viewing angles were <10° from the vertical direction.

3. Methods

Morisette et al. (2006) proposed a standard protocol for validating moderate scale (1 km) LAI products using field measurements (e.g. LAI-2200) combined with higher resolution (<30 m) remote sensing data. The commonly applied upscaling validation approach, as recommended by the CEOS LPV subgroup (Fernandes et al., 2014), was adopted in this study. The approach has three main steps (Fig. 2): (1) processing of high resolution images, (2) estimation of a reference LAI from the high resolution images, and (3) comparison of the moderate resolution LAI products with the upscaled high resolution reference LAI values. This procedure allows the construction of aggregated reference LAI maps to account for the spatial heterogeneity within the moderate resolution pixels.

Table 4

Information of the high resolution and the corresponding moderate resolution data used in the validation study^a. AOD: aerosol optical depth, DOY: day of the year, HR: high resolution, L7: Landsat 7, S2A: Sentinel-2A.

Date (DOY)	Sun zenith	Sun azimuth	View zenith	View azimuth	AOD	HR sensor	EPS (MM/DD)	GEOV2/PROBA-V	GLASS/GLOBMAP/MODIS/VIIRS (DOY)
(a) Honghe (12)									
2012/06/19 (171)	27.0	148.4	31.3	285.8	0.44	HJ-1B CCD1		06/20	169
2012/06/24 (176)	28.7	140.7	3.5	282.8	0.71	HJ-1A CCD1		06/20, 06/30	169
2012/06/29 (181)	30.9	133.8	23.1	98.8	0.30	HJ-1B CCD2		06/30	177
2012/07/19 (201)	30.1	147.5	30.4	285.8	0.37	HJ-1B CCD1		07/20	201
2012/07/25 (207)	33.5	133.1	32.3	97.7	0.07	HJ-1B CCD2		07/20, 07/31	201
2012/08/13 (226)	38.1	139.3	23.5	98.6	0.21	HJ-1B CCD2		08/10	225
2012/08/30 (243)	43.3	145.4	18.8	98.3	0.22	HJ-1B CCD2		08/31	241
2012/09/16 (260)	48.9	150.3	17.3	99.1	0.08	HJ-1B CCD2		09/10, 09/20	257
2013/06/24 (175)	33.1	127.9	9.3	99.2	0.38	HJ-1B CCD2		06/20, 06/30	169
2013/07/06 (187)	31.1	132.2	13.5	284.2	0.05	HJ-1B CCD1		06/30, 07/10	185
2013/07/15 (196)	34.8	128.7	8.0	97.6	0.15	HJ-1A CCD2		07/10, 07/20	193
2013/08/27 (239)	42.8	144.9	26.8	284.8	0.05	HJ-1A CCD1		08/31	233
(b) Hailun (11)									
2016/06/27 (179)	31.9	129.9	9.7	99.5	0.13	HJ-1B CCD2	07/05	06/30	177
2016/07/05 (187)	29.3	140.3	29.4	285.3	0.22	HJ-1A CCD1	07/05	06/30, 07/10	185
2016/07/14 (196)	32.1	135.1	12.1	284.3	0.06	HJ-1B CCD1	07/15	07/10, 07/20	193
2016/07/26 (208)	35.2	133.9	3.0	96.5	0.40	HJ-1B CCD2	08/05	07/20, 07/31	201
2016/07/31 (213)	33.8	142.6	30.3	285.9	0.15	HJ-1B CCD1	08/05	07/31	209
2016/08/02 (215)	31.8	157.7	6.1	301.5	0.45	S2A MSI	08/05	07/31, 08/10	209
2016/08/13 (226)	36.3	148.5	0.0	0	0.05	L7 ETM+	08/15	08/10	225
2016/08/20 (233)	40.3	142.6	8.0	284.5	0.06	HJ-1B CCD1	08/25	08/20	233
2016/08/29 (242)	41.0	152.9	0.0	0	0.05	L7 ETM+	09/05	08/31	241
2016/09/18 (262)	47.6	162.0	8.8	96.8	0.06	S2A MSI	09/25	09/10, 09/20	257
2016/09/22 (266)	50.6	152.6	8.3	284.5	0.29	HJ-1B CCD1	09/25	09/20, 09/30	265

^a Units for the sun zenith and azimuth and view zenith and azimuth angles are in degrees. The aerosol data are from the MODIS atmospheric L2 aerosol product (MOD04_L2.006). Note the EPS date in the file name corresponds to the last day of a 20-day compositing period, the GEOV2/PROBA-V date indicates the reference date (usually the middle) over a compositing window, and the GLASS/GLOBMAP/MODIS/VIIRS DOY marks the first day of an 8-day period in the naming.

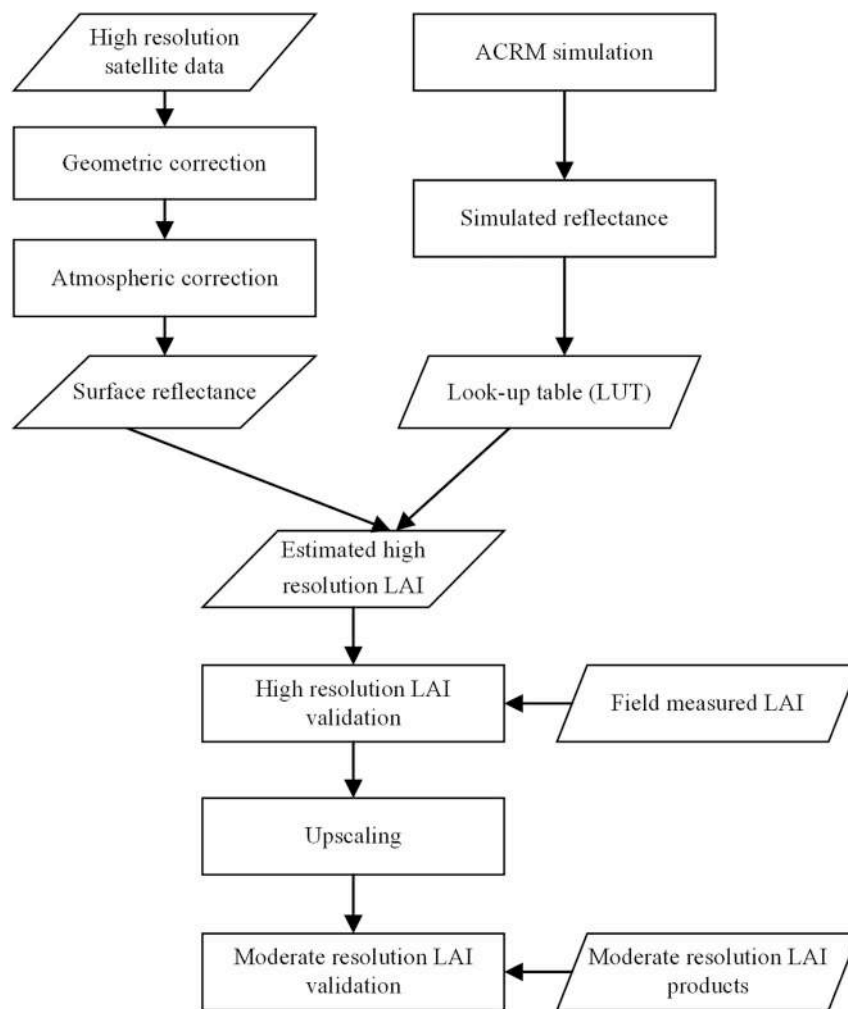


Fig. 2. Flow chart of the study.

3.1. Processing of HJ-1 data

All HJ-1 images were first rectified with second-degree polynomials to the Landsat 7 ETM+ images because of the same georeference system adopted by Landsat 7 and MODIS. At least 15 ground control points (GCPs) were used for each scene and the root mean square error (RMSE) is below 15 m (0.5 pixel). After registration, the HJ-1 raw radiance was atmospherically corrected and transformed to surface reflectance with the 6S (Second Simulation of the Satellite Signal in the Solar Spectrum) software (<http://6s.ltdri.org/>). 6S is an advanced radiative transfer code designed to simulate the reflection of solar radiation by a coupled atmosphere-surface system for a wide range of atmospheric, spectral, and geometrical conditions (Kotchenova et al., 2006; Vermote et al., 1997). A subarctic summer atmospheric model and a continental aerosol type were used to run 6S. The aerosol optical depth (AOD) data were obtained from the MODIS Level-2 atmospheric aerosol product (MOD04_L2.006) (Levy et al., 2015). Other parameters were set to the default values of the 6S input parameters. After atmospheric correction, the HJ-1 red and NIR reflectance data were first compared with the ground measured reflectance data over the Honghe area. Subsequently, the high resolution reflectance data were aggregated to 500 m and compared with the daily MODIS reflectances (MOD09GA, V6, 500 m) (Vermote, 2015). The MOD09GA daily product provides the reflectance data in 7 channels from 450 nm to 2100 nm from the MODIS sensor on board the Terra platform (Vermote, 2015).

3.2. Derivation of the high resolution reference LAI

In this study, the LUT approach was used to invert the LAI from the high resolution reflectance data in the red and NIR bands. The main advantage of the LUT inversion is its efficiency in the parameter prediction procedure (Darvishzadeh et al., 2008; Li and Fang, 2015). A turbid medium canopy reflectance model, ACRM (Kuusk, 2001), was first simulated to generate a database between canopy reflectance and various input parameters (Table 5). ACRM assumes a homogeneous layer of crop canopy and simulates the bidirectional canopy reflectance at 10 nm (Kuusk, 2001). The values of solar zenith and azimuth angles and view zenith and azimuth angles were extracted from the high resolution satellite products in Table 4. The Angstrom turbidity factor (β) was derived based on the variation of AOD (τ) with wavelength (λ , μm) (Ångström, 1961):

$$\tau(\lambda) = \beta * \lambda^{-k} \quad (2)$$

where k is a function of concentration and particle size distribution ($k \approx 1.4$). The same MODIS AOD product (MOD04_L2.006) used for HJ-1 atmospheric correction was also applied here (Levy et al., 2015). The angular distribution of leaves was assumed to be elliptical with an eccentricity of 0.98 and average leaf inclination angles (ALA) of 80° and 60° for paddy rice and other crops, respectively. The model sensitivity to the hot spot parameter is generally low for view directions that are away from the hot spot direction (Bacour et al., 2002). Therefore, the hot spot parameter was set as the average ($s_L = 0.5$) of the field values (Li et al., 2003). In ACRM, the spectra of leaf reflectance and

Table 5

Canopy, leaf, and soil parameters used for ACRM modeling of the surface reflectance. ALA: average leaf angle, LAD: leaf angle distribution, SLW: specific leaf weight.

	Parameters	Values	References
External parameters	Observation geometry	See Table 4	
	Angstrom turbidity factor (β)	Derived from Eq. (2)	
Canopy structure	Leaf area index (LAI)	0.01–8.0 by 0.02	
	Hot spot parameter (s_h)	0.5	Li and Fang (2015)
	Foliage clumping ($clmp$)	0.3–0.8 by 0.1	
	The regularity parameter (s_{zz})	1.0	Bai et al. (2017)
	Eccentricity of the LAD (e)	0.98	Fang et al. (2014, 2018)
	ALA of the elliptical LAD (θ_m)	80° (Honghe), 60° (Hailun)	Fang et al. (2014, 2018)
Leaf property	Effective # of layers in leaf (N)	1.55	Haboudane et al. (2004)
	Refraction index ratio of leaf surface wax to air (n_{ratio})	0.9	Kuusk (2001)
	Specific leaf weight (SLW, g/m ²)	60–200 by 20	Li et al. (2003)
	Leaf equivalent water thickness ($c1$, % of SLW)	130	Bai et al. (2017)
	Chlorophyll A & B ($c2$, % of SLW)	0.01–0.5 by 0.05	Li et al. (2003)
	Dry matter content ($c3$, % of SLW)	97	Houborg et al. (2007)
	Anthocyanins ($c4$, % of SLW)	0.2	Jiang et al. (2011)
Soil reflectance	Honghe (MOD09A1.006, 2,012,129)	B1 (0.620–0.670 μ m): 0.099 B2 (0.841–0.876 μ m): 0.148 B4 (0.630–0.680 μ m): 0.092 B5 (0.845–0.885 μ m): 0.177	This study
	Hailun (Landsat 8 OLI, 2016/6/2)		

transmittance are computed using the leaf optics model PROSPECT (Feret et al., 2008). The effective number of layers in a leaf (1.55) and the refraction ratio of leaf surface to air (0.9) were set to fixed values (Li et al., 2003). The chlorophyll content, leaf water thickness, dry matter content, and anthocyanins were selected as a percentage of the specific leaf weight (SLW) (Table 5).

The pre-season satellite reflectance data were used to represent the stationary background properties. The paddy rice fields in Honghe consist of a slab of water overlying the soil. The mean reflectance extracted from MODIS on May 8, 2012 (DOY 129), when the field was flooded, was used to represent the standardized background reflectance over the season. For the crops in Hailun, the Landsat 8 OLI reflectance on June 2, 2016, was used to represent the standardized background reflectance. This approach is similar to the method by Casanova et al. (1998) and the procedure in the Discrete Anisotropic Radiative Transfer (DART) simulation (Gastellu-Etchegorry et al., 2015). The total number of records in the database is over 608,000 and 438,000 for the Honghe and Hailun sites, respectively.

The LUT inversion process is based on a direct comparison of the observed satellite spectra and the simulated spectra through a cost function (J):

$$J = \sqrt{\frac{1}{N} \sum_{i=1}^N \left(\frac{\rho_i^{obs} - \rho_i^{sim}}{\rho_i^{obs}} \right)^2} \quad (3)$$

where N is the total number of bands used in the inversion ($N = 2$ for red and NIR bands), and ρ_i^{obs} and ρ_i^{sim} are the observed and simulated reflectance on band i , respectively. The first 100 records with the smallest J values were selected, and the corresponding LAI values averaged as the reference LAI for each pixel.

3.3. Evaluation and validation of the LAI products

Five LAI products have specific QQF and QQI layers embedded in the products (Table 3). The product quality control information was first explored. The LAI products from 2010 to 2017 were first inter-compared. The four companion MODIS products from different platforms and temporal composites, consisting of MCD15A2H (Terra + Aqua, 8-day), MCD15A3H (Terra + Aqua, 4-day), MOD15A2H (Terra, 8-day), and MYD15A2H (Aqua, 8-day), were also examined.

Using a bilinear interpolation method, the high resolution reference LAI data were spatially averaged to the corresponding spatial resolutions of different LAI products (Table 2). Subsequently, the moderate resolution LAI products were validated with the upscaled reference LAI

in a 3×3 pixel comparison mode that allows the effects of point spread function and geometric distortion to be limited. In addition, some alternative validation schemes were also investigated: (1) a direct pixel level comparison between the satellite LAI and the upscaled reference LAI for the corresponding pixels, (2) a site level comparison of the average satellite and field LAI values for the corresponding dates, and (3) a plot level comparison of the satellite and field LAI values averaged over the plots. The coefficient of determination (R^2), bias, RMSE, and relative RMSE (RRMSE) values were calculated for all the different schemes. During the procedure, cloudy pixels were masked out, and only good quality data were used in the validation (Table 3). For GEOV2, GLASS, and PROBA-V, only LAI data from the valid retrievals were considered (Table 3). The MODIS and VIIRS LAI data were extracted from the main retrieval algorithm. The EPS pixels marked as “no suspect” were included in the comparison, whereas all valid GLOBMAP retrievals were used. All comparisons were made based on the MODIS sinusoidal projection system.

4. Results

4.1. High resolution reference LAI

Fig. 3 shows that the high resolution HJ-1 reflectance agrees well with the field measured data over the Honghe area, with small bias (0.004) and RMSE values (0.05). The small underestimation of an outlier rice point (0.49, 0.33) is attributed to the scale differences between the field measurement and the HJ-1 pixel. The aggregated HJ-1 reflectance data show very high correspondence with the MODIS reflectance, with very high R^2 (> 0.93) and low bias (< 0.012) and RMSE (< 0.05) values for the Honghe and Hailun sites (Fig. 4). In most cases, the reflectance falls close to the 1:1 line. The relationship becomes more scattered for the NIR reflectance at the Hailun site from DOY 200 to 240 (Fig. 4b & c). This observation is mainly attributed to the mixed ground cover types revealed in the high resolution images.

The high resolution LAI data estimated from the HJ-1 WVC, Landsat 7 ETM+, and the Sentinel-2A MSI reflectance data are shown in Fig. A1. The seasonal and spatial variation of the LAI is obvious from the figure. At the Honghe site, the spatial LAI distribution in 2013 is similar to that in 2012; however, the start of the growing season is slightly later in 2013 than that in 2012 (Fig. A1a). The LAI values of roads, ditches, and residential areas are generally low. These effects are more pronounced in the Hailun maps (Fig. A1b).

The high resolution LAI data are consistent with the field measured LAI, characterized by a slope close to the 1:1 line (Fig. 5). The high

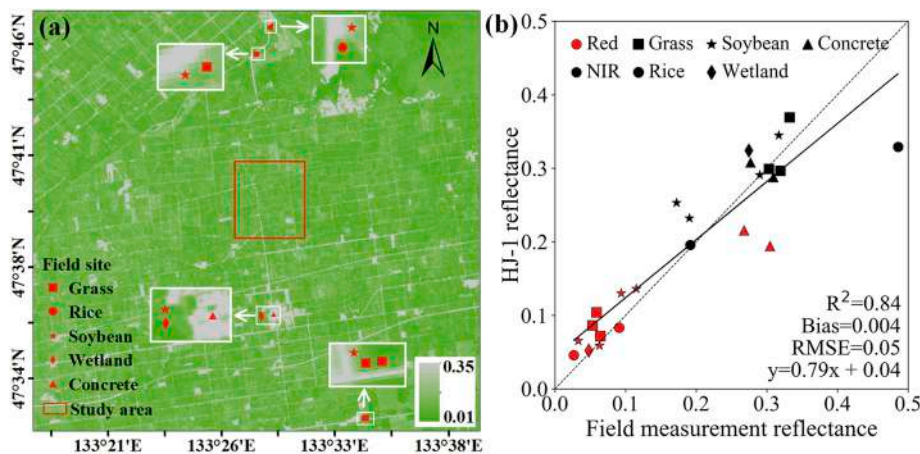


Fig. 3. Comparison of the HJ-1 reflectance with field measurements. (a) Location of the field measurements over the Honghe area. The background is an HJ-1 reflectance image (red band, 630–690 nm) on June 24, 2013. (b) Scatterplot between the HJ-1 reflectance and field measurements. See Table A1 for more details about the data. (For interpretation of the references to color in this figure legend, the reader is referred to the web version of this article.)

resolution LAI is an average of the 3×3 pixels corresponding to the field plot locations (Table 1). The statistical results show an R^2 of 0.81 and 0.86, and RMSE of 0.62 and 0.70 for the Honghe and Hailun sites, respectively. The smaller RMSE value at the Honghe site is attributable to the more homogeneous rice crops (Fig. 5a). At the Hailun site, the high resolution LAI slightly overestimates during the peak growing season in July, but it underestimates in September, when the leaves in some places have become senescent. When all crops are combined, the high resolution LAI shows excellent agreement with the field measured LAI ($R^2 = 0.85$ and $RMSE = 0.66$) (Fig. 5c).

4.2. Product quality control information

Fig. 6 shows the percentage of LAI retrievals in different quality status, as indicated by the QQF. The figure shows a clear seasonal pattern. The suspected retrievals for EPS are mainly located between DOY 100 and 200 at the Honghe site, whereas only a small portion of the pixels are marked with “suspect” at the Hailun site, mainly during the rapid growth period. Almost all GEOV2 retrievals are considered “valid” over the years, except for a short period in 2015. For PROBA-V, nearly all retrievals are labeled “valid” from DOY 100 to 300 and “invalid” for the other periods. The MODIS QQF shows that nearly all the LAI values are retrieved by the main algorithm during the beginning and ending of the season. The fraction of the main algorithm retrievals is significantly lower in July and August, with large swings between DOY 180 and 250. During this period, the empirical backup algorithm is mainly used, and occasionally, there are no valid retrievals. VIIRS shows similar seasonal patterns as MODIS, with lower quality during the summer. There is more variation in VIIRS than in MODIS between DOY 150 and 250, and the percentage of the main retrievals is $\sim 10\%$

lower than those of the MODIS.

The product QQI values provide theoretical quantification of the uncertainties in the LAI products (Fig. 7). The absolute uncertainties are consistently higher during the peak growing season and lower during the beginning and ending of the season (Fig. 7a and b). The higher QQI values during the summer are related to the higher LAI values during this period. The differences between the products are very obvious. The average QQI values for EPS, GEOV2, and PROBA-V are generally higher than those of MODIS and VIIRS. In contrast to the absolute uncertainties, the relative uncertainties are generally lower during the peak growing season than the other periods (Fig. 7c and d). The relative QQIs values are higher during the early growing period than the late period. Similar to the absolute QQI values, the relative QQI values for EPS, GEOV2, and PROBA-V are also higher than those of MODIS and VIIRS. VIIRS shows the lowest relative QQI, and EPS shows unusually high spikes during the LAI growing period.

4.3. Inter-comparison of the LAI products

The spatial distribution of all LAI products is illustrated in Fig. A2. The figure shows that EPS, GEOV2, and GLASS are generally more homogeneous than the other products in both the Honghe and Hailun sites. PROBA-V shows more details than the other products because of its higher resolution (300 m). Fig. 8 shows the temporal progression of the LAI products from DOY 100 to DOY 300. All LAI products show similar seasonal patterns, depicting the seasonality of the crops very well, with a rapid increase in LAI around DOY 150–200 and a gradual decrease around DOY 240–300. Benefiting from the use of various gap filling techniques, GEOV2, GLASS, GLOBMAP, and PROBA-V show smoother temporal profiles than EPS, MODIS and VIIRS.

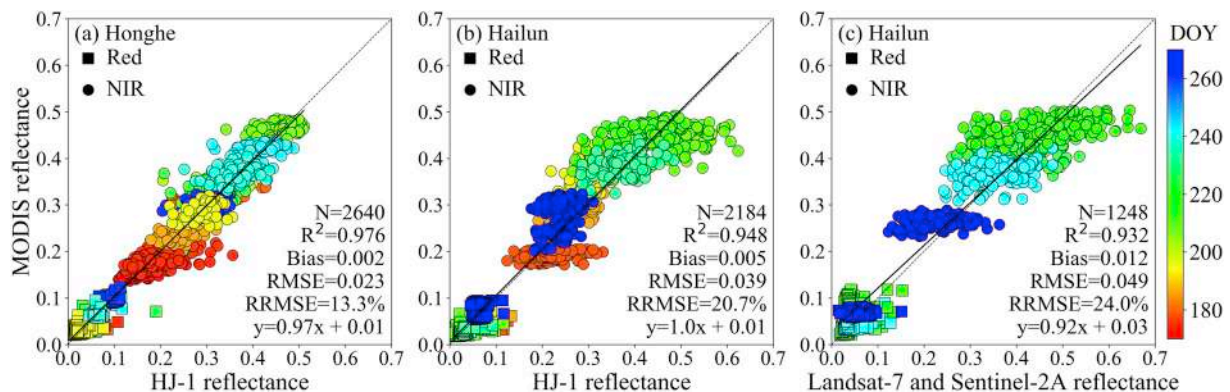


Fig. 4. Comparison of the aggregated high resolution reflectance data with the MODIS reflectance data (MOD09GA, V6) for HJ-1 in Honghe (a) and Hailun (b) and Landsat-7 and Sentinel-2A in Hailun (c). The color bar indicates different observation dates.

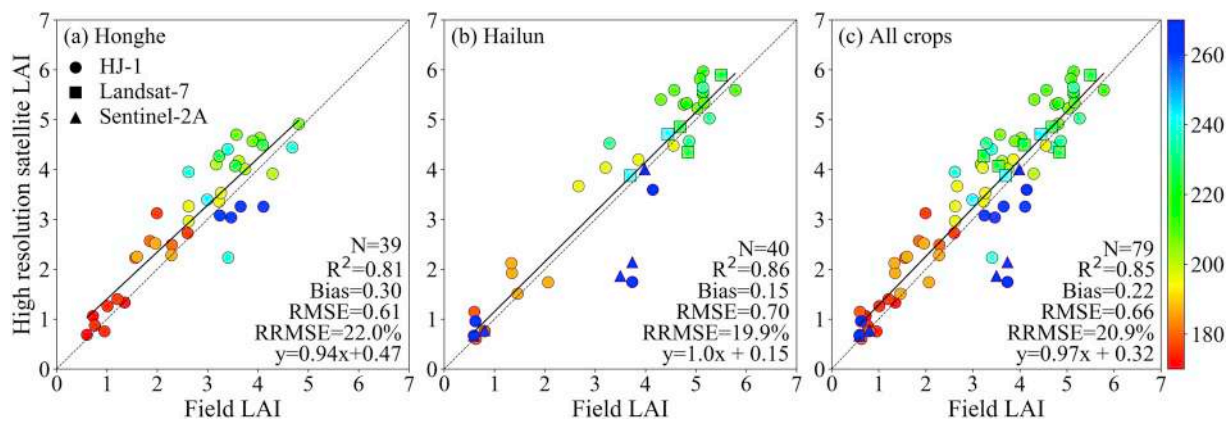


Fig. 5. Comparison of the high resolution reference LAI (3×3 pixels) with the field measured data for paddy rice in Honghe (a), maize, soybean, and sorghum in Hailun (b), and all crops (c). The colors represent different observation dates.

The LAI profiles differ through the growing season (Fig. 8). The largest discrepancies (up to 3.0–4.0) occur from DOY 180 to 260. EPS shows a delayed profile than the other products, especially in 2017. GLASS shows the smoothest pattern, but the smallest value. Moreover, the average LAI decreasing period estimated with GLASS is later than most of the other products, except for EPS. GLOBMAP is generally higher (1–2) than the other products, and for the paddy rice, the start of the LAI increase is about one month earlier than the other products.

The LAI products shows similar temporal patterns at both the Honghe and Hailun sites (Fig. S1). The products show different profiles across the years as a result of different weather conditions, and planting and management practices. The largest differences occur during the peak growing season. GLASS shows the least annual variation (<0.5) during the peak growing season, followed by GEOV2 (~ 1.0). GLOBMAP (4.0), MODIS (3.0), and VIIRS (2.5) show the highest variation during the peak growing season. For EPS and PROBA-V, the variation

across the different years is around 1.5. Over the Hailun site, PROBA-V shows a lower LAI peak (~ 4.0) in 2014, whereas GLOBMAP shows a lower peak (~ 5.0) in 2013.

The LAI values derived from the four companion MODIS products were compared (Fig. 9). The four MODIS products are derived from different compositions of the MODIS sensors onboard the Terra and Aqua satellites for 8- and 4-day time steps. The 4-day joint platform product, MCD15A3H, is much more variable than the other three 8-day products, especially over the rice field. The single platform 8-day products, MOD15A2H (Terra) and MYD15A2H (Aqua), are much lower (~ 2.0) from DOY 180 to 240. The underestimation effects were largely removed in the joint platform 8-day product, MCD15A2H. Therefore, the MCD15A2H (Terra + Aqua, 8-day) was used to represent the MODIS LAI throughout this paper.

The LAI products were composited monthly and compared with the MODIS LAI (Fig. 10). EPS shows the weakest correlation with MODIS

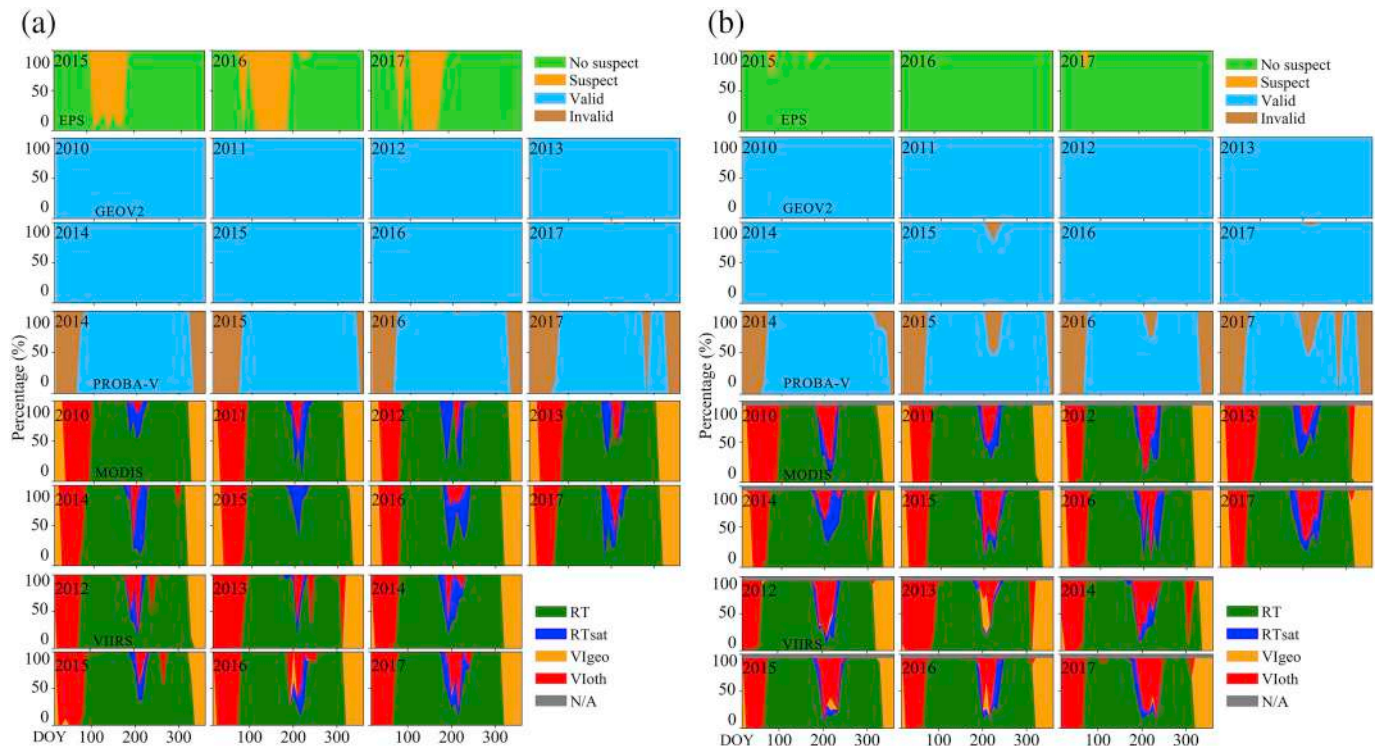


Fig. 6. Temporal variation of LAI qualitative quality flags (QQFs) over Honghe (a) and Hailun (b) for different years. DOY: day of year; RT and RTsat: main radiative transfer (RT) method used with the best result and with saturation, respectively; VIgeo and VIoth: empirical vegetation index (VI) algorithm used due to bad geometry and other problems, respectively; N/A: no valid retrieval.

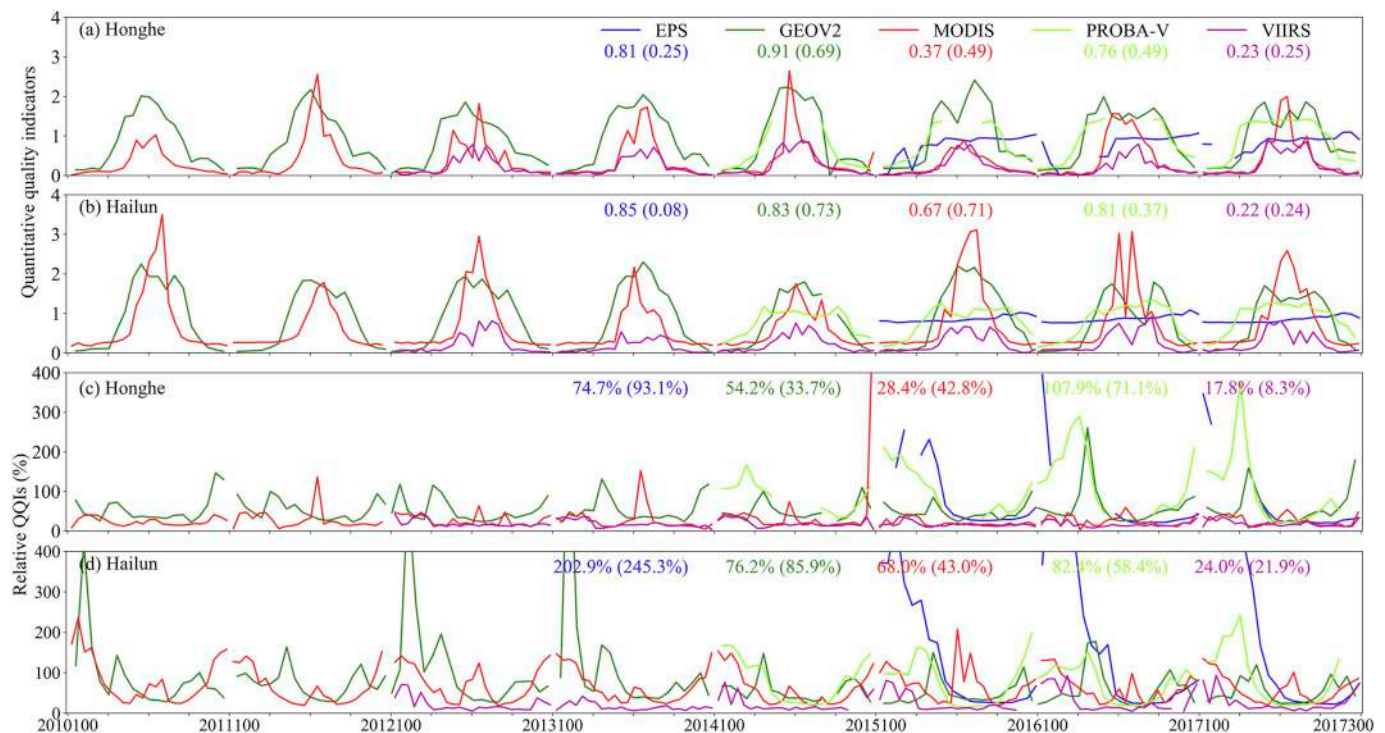


Fig. 7. Temporal variation of LAI quantitative quality indicators (QQIs) and relative QQIs (%) between DOY (day of year) 100 and 300 from 2010 to 2017. The relative QQI is calculated as a ratio of the QQI and the average LAI (Fig. 8). The numbers are the average (standard deviation) values over the period.

($R^2 < 0.10$, $RMSE > 1.70$). GEOV2 correlates well with MODIS ($R^2 > 0.80$, $RMSE < 1.15$), but it overestimates the latter in the paddy rice (bias = 0.93). GLASS has a moderate correlation with MODIS (R^2 : 0.60–0.66, $RMSE$: 0.73–0.77), but it shows some unexpected plateau values in July (3.5), August (4.5), and September (2.0), respectively. GLOBMAP significantly overestimates MODIS, especially in August and

September (> 2.0). PROBA-V has a good agreement with MODIS ($R^2 > 0.67$, $RMSE < 0.77$), but it slightly overestimates in July and August. As expected, VIIRS shows the best correlation with MODIS with $R^2 > 0.68$ and $RMSE < 0.54$.

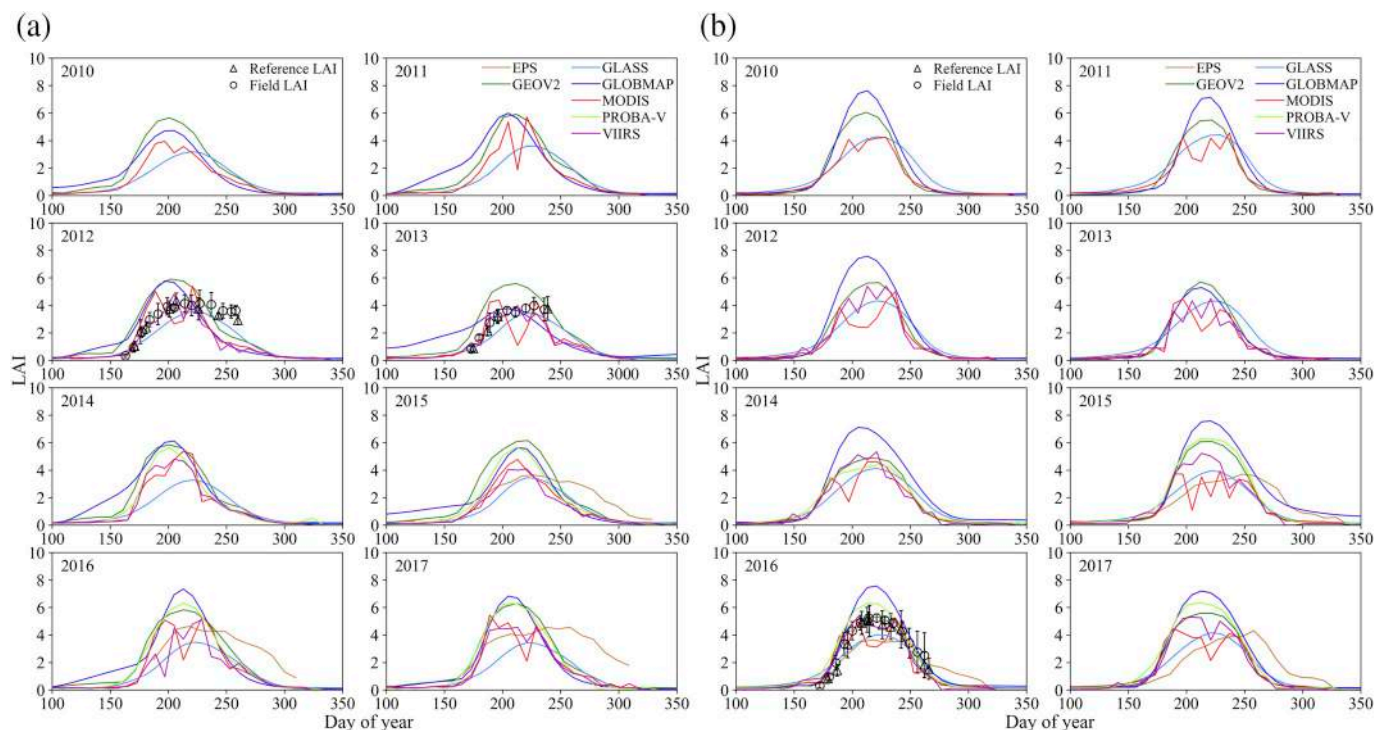


Fig. 8. Temporal variation of the moderate resolution LAI products in Honghe (left) and Hailun (right). The reference (triangles) and field (circles) LAI values are marked with standard deviation ranges. The temporal profiles were shifted to match the reference dates because of the different dates in the file names (Table 4).

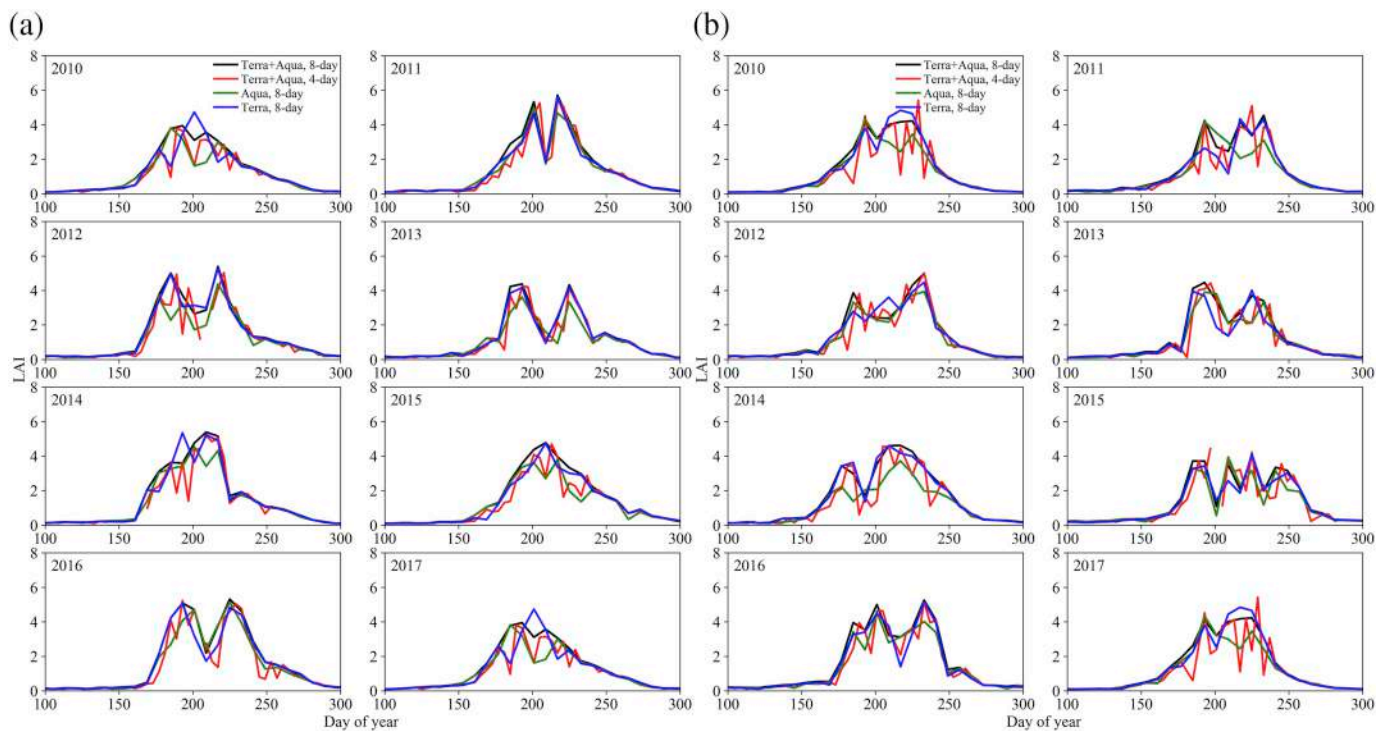


Fig. 9. Comparison of the MODIS LAI product suites (version 6): MCD15A2H (Terra + Aqua, 8-day), MCD15A3H (Terra + Aqua, 4-day), MOD15A2H (Terra, 8-day), and MYD15A2H (Aqua, 8-day), over Honghe (a) and Hailun (b) (2010–2017).

4.4. Validation of the LAI products

Fig. 11 validates the moderate resolution LAI products with the upscaled reference LAI. The figure shows huge variations among different products, with the RMSE varies between 0.8 and 2.0, and the RRMSE between 25 and 60%. The performance of the products at the Hailun site is generally better than that at the Honghe site, as displayed by the higher R^2 values in the former. Nearly all LAI products, except

for GLASS, fail to depict the expected variability of the reference LAI ($R^2 < 0.30$) at the Honghe site. At the Hailun site, GEOV2, GLOBMAP, and PROBA-V overestimate the reference LAI, and the other four products underestimate.

The products show weaker performance during periods of rapid changes in LAI: the products tend to overestimate the reference LAI before DOY 200 and underestimate after DOY 240 (Fig. 11). The performance is highly variable during the peak growing season. Between

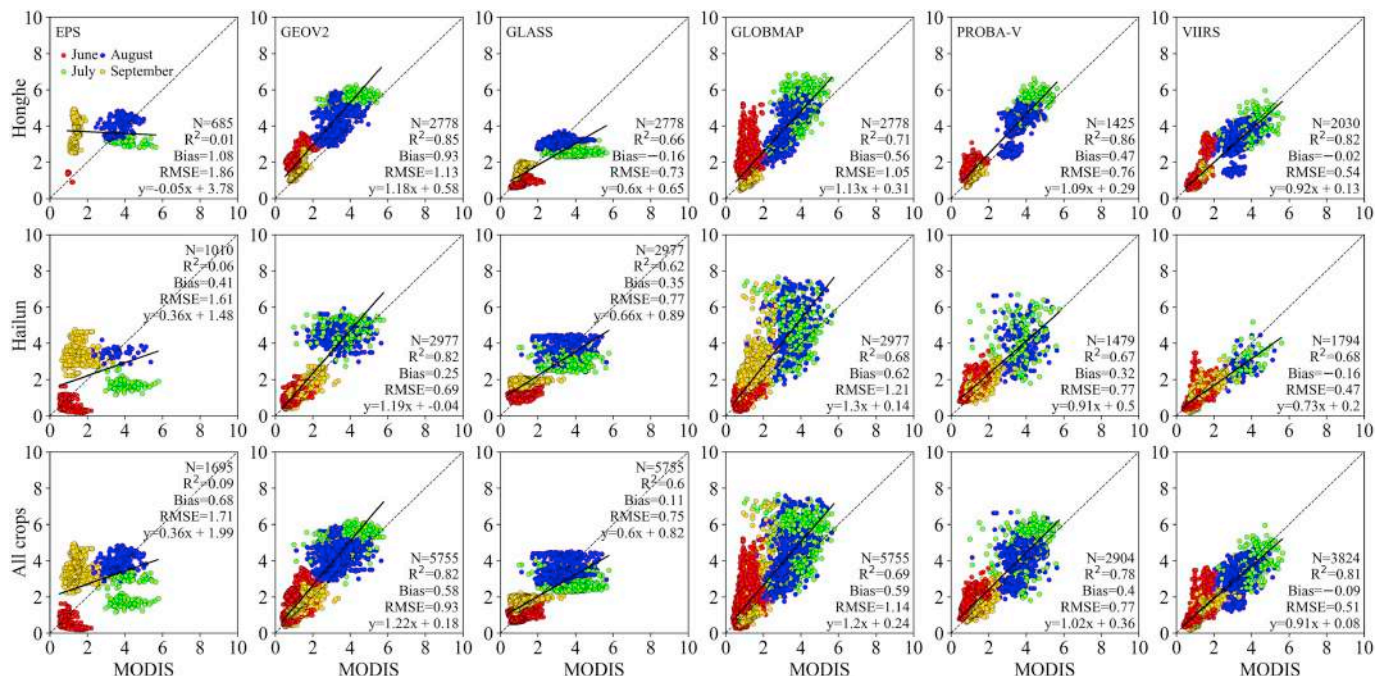


Fig. 10. Comparison of the monthly composited LAI with MODIS for paddy rice in Honghe (first row), maize, soybean, sorghum in Hailun (middle row), and all crops in both areas (bottom row).

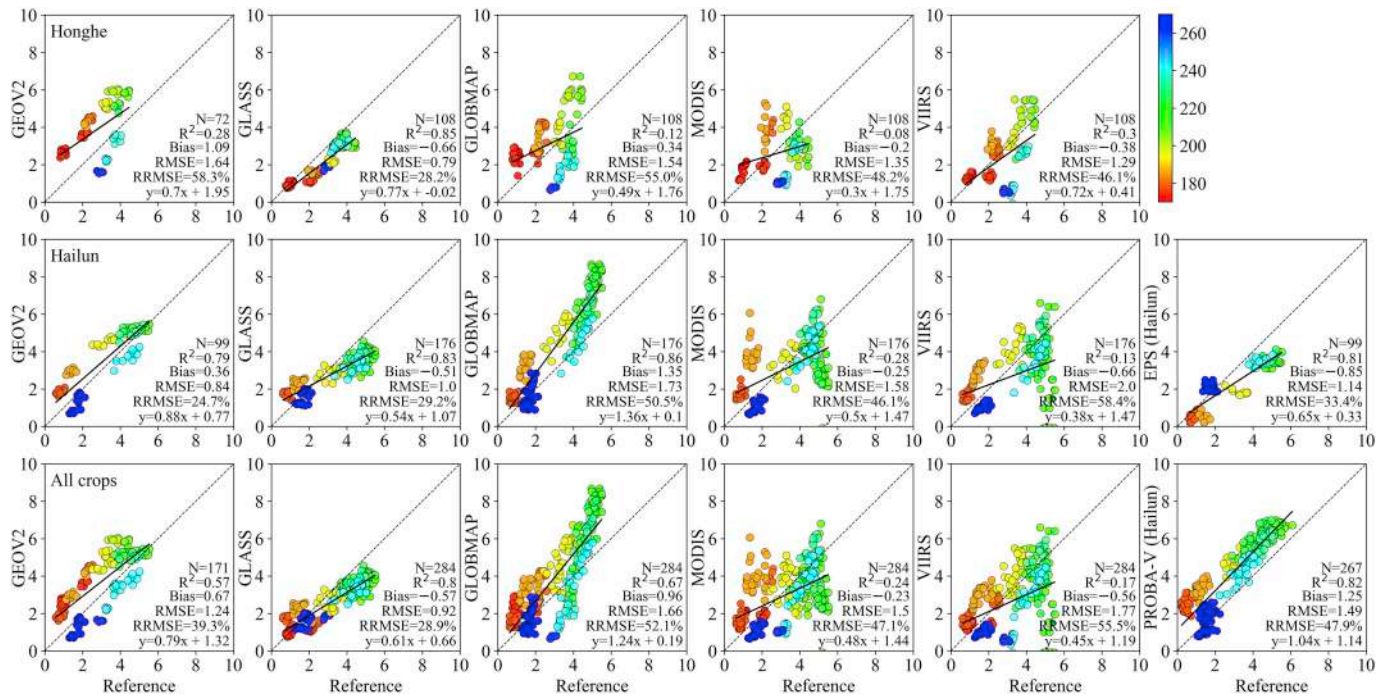


Fig. 11. Comparison of the moderate resolution LAI products with the upscaled reference LAI (3×3 pixels) at the Honghe (first row), Hailun (middle), and both sites (bottom). The right most column compares for EPS and PROBA-V over Hailun. The color bar indicates different observation dates.

DOY 200–240, the LAI ranges from 4.0 to 8.0 (GLASS to GLOBMAP) at the Honghe site and from 4.0 to 9.0 (EPS to GLOBMAP) at the Hailun site. During this period, GEOV2, GLOBMAP, and PROBA-V products overestimate the reference LAI, GLASS underestimates, and the MODIS and VIIRS values are highly scattered. During the late growing season after DOY 240 (bluish points), the products underestimate the reference LAI, except for EPS, which slightly overestimates. Among the seven products, five products (excluding EPS and GLASS) overestimate at the Hailun site.

EPS shows a good correspondence with the reference LAI ($R^2 = 0.81$), but it greatly underestimates (bias = -0.85) at the Hailun site, especially at the peak growing season (Fig. 11). GEOV2 shows a poor correspondence at the Honghe site ($R^2 = 0.28$, RMSE = 1.64), but the performance is much better at the Hailun site ($R^2 = 0.79$, RMSE = 0.84). GLASS consistently underestimates at the two sites but shows the smallest RMSE and RRMSE values (0.92 and 28.9% for all crops) among all products. Although GLOBMAP shows the best correspondence ($R^2 = 0.86$) with the reference LAI, the product displays the largest overestimation (bias = 1.35) at the Hailun site. MODIS and VIIRS show high accuracy (bias < 0.6), but they also exhibit high uncertainties (RMSE ≥ 1.5) at both sites. PROBA-V systematically overestimates at the Hailun site (bias = 1.25), and also displays high uncertainties (RMSE = 1.49, RRMSE = 48%).

In addition to the 3×3 pixel comparison, the results of the alternative comparisons made at the pixel, site, and plot levels were investigated (Figs. S2–S4). Generally, there is no significant difference among the different validation schemes (Table 6). The statistics show that the overall median R^2 , RMSE, and RRMSE values are about 0.50, 1.46 and 48%, respectively, for all crops. Similarly, the table shows better correspondence at the Hailun site than at the Honghe site, with much higher R^2 values (0.74 vs. 0.22). At the Honghe site, the 3×3 comparison shows the best correspondence with median $R^2 = 0.28$, RMSE = 1.35, and RRMSE = 48.2%. At the Hailun site, the site level comparison shows the best agreement, with median $R^2 = 0.85$, RMSE = 1.10, and RRMSE = 33.6%.

Fig. 12 shows the histogram distribution of all valid LAI values from the high resolution reference data and the moderate resolution LAI

products. The histogram distributions significantly differ between the products and no product could fully explain the reference distributions at both sites. The differences between the products are also illustrated in the LAI profiles for specific days (color profiles in Fig. 12). For the Honghe site, the reference LAI values range between 0.5 and 6.0, with local peaks around 1.5 and 3.0. Similar distributions in peak values are found for GLASS, MODIS, and VIIRS, whereas GEOV2 shows equalized distribution for LAI between 1.5 and 6.0. GLASS shows systematic underestimation with two narrow peaks centered around 1.5 and 3.0. At the Hailun site, the reference LAI ranges between 0 and 6.0, with two symmetrical peaks between 0 and 3 and 3–7, and a low valley around 3.0. Only GLOBMAP shows a similar pattern to the reference, whereas all the other products show skewed LAI distributions. For example, GEOV2 shows a high LAI peak between 5.0 and 5.5. The ranges of EPS and GLASS are rather narrower than the reference LAI. In contrast, PROBA-V shows much higher LAI values (4.0–7.0) than the reference data.

5. Discussions

5.1. LAI product quality

The time series validation results reveal remarkable uncertainties (RMSE > 0.8 and RRMSE $> 25\%$) among current LAI products for agricultural crops in northeastern China (Fig. 11). The product quality depends, to a large extent, on the specific stage of the growing season, because of the different retrieval methodology and the quality of input data. During the green-up period, the LAI products tend to overestimate the reference LAI of the crops; however, the products underestimate the crop LAI during the senescence stage. The higher uncertainties during the green-up and senescence periods complement other validation findings from croplands (Campos-Taberner et al., 2018; Casa et al., 2012; Jégo et al., 2012). On the other hand, the product quality varies significantly during the maturity stage, mainly because of the impact of cloud contamination and algorithm saturation issues. The higher discrepancies indicate that current global LAI retrieval algorithms are still limited in capturing the temporal variation of plant properties at a

Table 6

Different validation schemes of the satellite LAI products with high resolution reference LAI and field measured LAI values. The median values all shown in italics for Honghe (a), Hailun (b), and all crops (c). The data are from Figs. 12, S2–S4, respectively. RMSE: root mean square error, RRMSE: relative RMSE (%).

LAI products	3 × 3 pixel comparison			Direct pixel comparison			Site level comparison			Plot level comparison			Medians		
	R^2	RMSE	RRMSE	R^2	RMSE	RRMSE	R^2	RMSE	RRMSE	R^2	RMSE	RRMSE	R^2	RMSE	RRMSE
(a) Honghe															
GEOV2	0.28	1.64	58.3	0.25	1.71	61.4	0.12	1.87	66.5	0.19	1.85	59.9	0.22	1.78	60.7
GLASS	0.85	0.79	28.2	0.78	0.82	29.4	0.62	1.02	36.3	0.66	0.99	32.1	0.72	0.91	30.8
GLOBMAP	0.12	1.54	55.0	0.12	1.64	58.9	0.07	1.65	58.7	0.03	1.82	59.0	0.10	1.65	58.8
MODIS	0.08	1.35	48.2	0.06	1.51	54.3	0.01	1.57	55.9	0.13	1.55	50.2	0.07	1.53	52.3
VIIRS	0.30	1.29	46.1	0.29	1.31	48.2	0.20	1.43	50.9	0.19	1.52	49.3	0.25	1.37	48.8
<i>Medians</i>	0.28	1.35	48.2	0.25	1.51	54.3	0.12	1.57	55.9	0.19	1.55	50.2	0.22	1.53	52.3
(b) Hailun															
EPS	0.81	1.14	33.4	0.75	1.22	35.7	0.79	1.10	31.4	0.45	1.55	44.2	0.77	1.18	34.6
GEOV2	0.79	0.84	24.7	0.75	0.93	27.2	0.85	0.86	27.0	0.53	1.26	36.0	0.77	0.90	27.1
GLASS	0.83	1.00	29.2	0.67	1.14	33.3	0.86	0.87	27.3	0.69	1.19	34.0	0.76	1.07	31.3
GLOBMAP	0.86	1.73	50.5	0.79	1.88	55.0	0.92	1.80	56.5	0.68	1.77	50.5	0.83	1.79	52.8
MODIS	0.28	1.58	46.1	0.21	1.81	56.1	0.44	1.23	38.6	0.35	1.59	45.4	0.32	1.59	45.8
PROBA-V	0.82	1.49	47.9	0.67	1.62	53.9	0.85	1.42	44.5	0.45	1.65	47.1	0.75	1.56	47.5
VIIRS	0.13	2.00	58.4	0.43	1.39	49.1	0.57	1.07	33.6	0.42	1.47	41.9	0.43	1.43	45.5
<i>Medians</i>	0.81	1.49	46.1	0.67	1.39	49.1	0.85	1.10	33.6	0.45	1.55	44.2	0.74	1.44	45.2
(c) All crops															
GEOV2	0.57	1.24	39.3	0.53	1.31	41.5	0.44	1.48	49.5	0.29	1.65	50.8	0.49	1.40	45.5
GLASS	0.80	0.92	28.9	0.70	1.02	32.4	0.70	0.95	31.8	0.66	1.07	32.9	0.70	0.99	32.1
GLOBMAP	0.67	1.66	52.1	0.59	1.78	56.6	0.49	1.72	57.5	0.31	1.80	55.4	0.54	1.75	56.0
MODIS	0.24	1.50	47.1	0.17	1.67	55.4	0.21	1.42	47.5	0.24	1.57	48.3	0.23	1.54	47.9
VIIRS	0.17	1.77	55.5	0.37	1.35	48.6	0.37	1.27	42.5	0.31	1.50	46.2	0.34	1.43	47.4
<i>Medians</i>	0.57	1.50	47.1	0.53	1.35	48.6	0.44	1.42	47.5	0.31	1.57	48.3	0.49	1.46	47.9

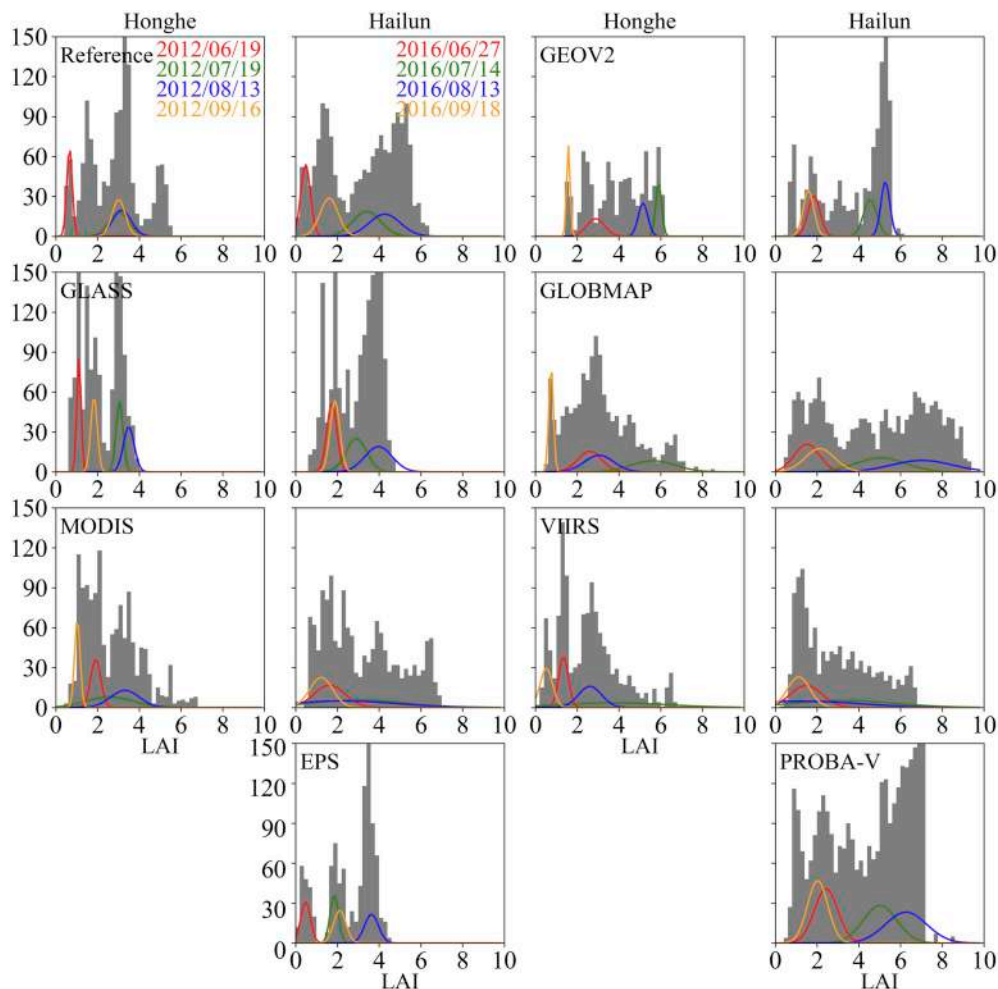


Fig. 12. Histogram of the upscaled resolution reference LAI (500 m) and the moderate resolution LAI products for Honghe (left) and Hailun (right). The colored profiles show the typical profiles over four days (Table 4). (a).

regional scale.

As a result of different input reflectances and retrieval algorithms, distinct differences exist among the different LAI products. The small negative bias for EPS during the peak growing season is partly attributed to the lack of representation of the clumping effect at the canopy level in the algorithm (García-Haro et al., 2018). Both GEOV2 and PROBA-V overestimate the reference data (Fig. 11). Overestimation of the reference data has also been reported in the earlier GEOV1 product over crops (Camacho et al., 2013). One reason for the overestimation is possibly due to the lack of representative inputs (e.g., for the soil reflectance) within the neural network training database, especially over the paddy rice site. As shown in Fig. 11, GEOV2/PV (1/112°) matches better than PROBA-V (300 m) with the upscaled reference LAI at the Hailun site. The systematic overestimation of PROBA-V (bias = 1.25) is mainly attributed to two reasons: (1) the usage of the blue band, which is sensitive to atmospheric effects, and (2) the usage of the top of aerosol reflectance after partial atmospheric correction as the input data (Baret et al., 2016).

Compared with the reference LAI, GLASS shows the least uncertainty (RMSE = 0.92 and RRMSE = 28.9% for all crops) among all products (Fig. 11). Part of the lower uncertainty is attributed to the general underestimation of the GLASS LAI for all crops (bias = -0.57). The GLASS algorithm makes use of the MODIS reflectance for an entire year to estimate the yearly LAI profile (Xiao et al., 2014). The high bias may also be related to the limited training data over croplands, especially during the summer.

GLOBMAP significantly overestimates the reference LAI (bias = 1.35) at the Hailun site and displays high bias (0.96) and RMSE values (1.66) for all crops (Fig. 11). However, other studies have shown that GLOBMAP generally underestimates GLASS, GEOV1, and MODIS (V5) for crops at a global level (Fang et al., 2013). GLOBMAP classifies all herbaceous land cover types as crops and grasses, and LAI is estimated with an empirical relationship with the simple ratio (SR) vegetation index for these types (Liu et al., 2012). The significant overestimation of GLOBMAP in this study is attributed to the lack of generality of the global LAI algorithm over the study area.

Earlier studies have found that MODIS (V5) generally underestimates for crops (~0.5), especially during the senescence stage (Camacho et al., 2013; Claverie et al., 2013; Yan et al., 2016b). In this study, the newer MODIS V6 shows a smaller bias (0.17) but similar underestimation during the senescence period (Fig. 11). The bias of MODIS V6 could reach 4.0 during the green-up stage (Fig. 11). Similar poor performance, although to a lesser extent, has been reported for earlier versions of MODIS (Baret et al., 2013; Groenendijk et al., 2011). VIIRS agrees well with MODIS ($R^2 = 0.81$, RMSE = 0.51, Fig. 10), but both products show high uncertainties when compared with the reference LAI of the crops (RMSE > 1.5, RRMSE > 47%, Fig. 11). The high uncertainties may also be attributable to the variable input reflectance, especially during the peak growing season.

Current LAI products show much higher correspondence with the reference LAI for the maize, soybean, and sorghum crops at the Hailun site than for the paddy rice at the Honghe site (Fig. 11 & Table 6). The poorer performance of LAI products over rice fields has been reported in earlier studies (Cheng, 2008; Urrutia, 2010). For example, Urrutia (2010) reported that MODIS (V5) could underestimate the rice LAI by about 1.0 to 3.0. This study shows a similar underestimation of LAI in a paddy rice site for GLASS, MODIS (V6), and VIIRS, especially when the LAI > 3.0 (Fig. 11). Recently, Campos-Taberner et al. (2018) reported that EPS, GEOV1, and MODIS (V5) performed very well for rice crops in southern Europe ($R^2 \geq 0.90$ and RMSE ≤ 0.80). However, our results show that GEOV2, a successor of GEOV1, overestimates the reference LAI of rice crops by >1.0 (Fig. 11). It is noted that, in contrast to the single rice crop in Honghe, all maize, soybean, and sorghum crops were combined and compared together with the reference LAI at the Hailun site.

5.2. Perspectives

A comparison of the product quality flags shows that the GPR algorithm, adopted by EPS, may be more affected by the background issues during the green-up period (Fig. 6). However, the EPS algorithm effectively manages the cloud contamination issues during the summer, by adopting the SWIR band. In contrast, the MODIS LUT algorithm is more stable during the green-up period, but it suffers from the low-quality input data during the summer.

Although the product theoretical uncertainties, i.e., the QQI, have been available over the past decade (e.g., MODIS), the QQI information has been rarely investigated in the community. The seasonal variation of the product QQI is valuable as it allows users to understand which temporal periods are more or less dispersible (Fig. 7). The time series of the QQI can be examined to determine the temporal evolution of the product quality. However, because of algorithm differences, current QQI information is incomparable across different products and cannot be used to evaluate which product is less uncertain. The use of a well-defined standard QQI is desirable to allow inter-comparison across different products.

This study highlights the challenges in estimating LAI from moderate resolution satellite data at different growth stages. The poorer performance of the LAI products at the Honghe site illustrates the need to consider the background effects in regional scale LAI mapping. Inadequate consideration of the water-logging environment in radiative transfer models has caused large uncertainties in the LAI estimation in rice fields (Urrutia, 2010; Wu et al., 2006; Xiao et al., 2006). At the Hailun site, the leaf senescence and background exposure during the late stage may have contributed to the underestimation of LAI in both high and moderate resolution LAI data (Figs. 5 and 12). Duveiller et al. (2011), using SPOT sensors (20 m), reported similar high uncertainties (RRMSE > 100%) in estimating the winter wheat LAI during the senescent phase. This study used the pre-season surface reflectance as the background reflectance in the ACRM simulation process. Indeed, the model simulation and LAI retrieval can be improved by incorporating a more advanced soil model (e.g., Jiang and Fang, 2019) or using the real-time background reflectance from the field. A physically more plausible way is to use crop specific radiative transfer models (Richter et al., 2011).

There is generally no significant difference among the four different validation schemes investigated in this study (Table 6). The 3 × 3 comparison scheme was applied in this study because it suppresses the effects of point spread function and registration errors. The direct pixel level comparison reveals the differences between the product and the reference LAI, but it may be affected by the spatial heterogeneity within the pixel. A comparison of the average values for different dates minimizes the random errors relative to the systematic errors. A sufficient number of data pairs over the whole time series are necessary to apply the site level comparison properly. The plot level comparison is easy to apply for diagnostic purpose, but it requires that the study area is homogeneous and the plot measurements are representative of the pixel values.

The high spatial resolution LAI data generated from HJ-1, Landsat, and Sentinel-2A provide a good opportunity to evaluate the global moderate resolution products over time. Fig. 5 shows that the uncertainty of the high resolution reference LAI (RMSE = 0.66 for all crops) is about 44% of the uncertainties of the LAI products (median RMSE ≈ 1.50 , Table 6). For a proper validation of the LAI products, the standard uncertainty of the reference data should ideally not exceed 30% of the product uncertainty (Widlowski, 2015). Obviously, the uncertainty of the reference LAI is about 50% higher than the ideal tolerance level in this study. Uncertainties in the reference data arise from the fact that crop fields are not perfectly homogeneous (e.g., bare soils, paved roads, and ditches), at both the high- and moderate-resolution pixel levels. The land cover heterogeneity could certainly affect the field LAI sampling, measurement and spatial averaging, the

observed satellite reflectance, and the LAI retrievals. It is noted that LAI-2200 obtains the PAI_{eff} , which may overestimate the true LAI because of the impact of leaf senescence and crop stems, especially during the late growing season (e.g., Fig. 5b). Nevertheless, we do not expect the spatial heterogeneity and the uncertainties in the LAI measurements to significantly impact the main conclusions drawn from this study.

6. Conclusion

A time series validation study was performed for seven global LAI products over the croplands in northeastern China. The validation study reveals remarkable uncertainties in current LAI products for agricultural crops (RMSE: 0.80–2.0 and RRMSE: 25–60%). The performance of the LAI products varies at different phenological stages: the global LAI tends to overestimate the high resolution reference LAI during the green-up stage, largely fluctuates during the maturity stage, and underestimates during the senescence stage. The weak performance is mainly attributed to the lack of regional tuning of the global LAI algorithms over agricultural areas. Further efforts are necessary to improve the LAI product quality in local and regional scales, especially for the water-logged paddy rice fields. This study highlights the importance of crop-specific and temporal validation at a regional scale. More validation studies are needed in other parts of the world with

sufficient field LAI measurements. The uncertainty information exposed in this study is beneficiary for product improvement and the application community.

Acknowledgments

This study was performed under the framework of CEOS/LPV (<https://lpvs.gsfc.nasa.gov/>). Funding to the study has been provided by several projects: data analysis and manuscript preparation by the National Key Research and Development Program of China (2016YFA0600201), field campaigns and data collection by the National Natural Science Foundation of China (41471295, 41171333, 41531174), and hardware procurement by the Hundred Talent Program of the Chinese Academy of Sciences. The field measured and high resolution reference LAI data are available from PANGAEA (<https://doi.pangaea.de/10.1594/PANGAEA.900090>). We thank CRESDA (<http://www.cresda.com/EN> or <http://218.247.138.119:7777/DSSPlatform/index.html>), USGS EarthExplorer (<https://earthexplorer.usgs.gov/>), and ESA Copernicus Open Access Hub (<https://scihub.copernicus.eu/dhus/#/home>) for providing the HJ-1, Landsat 7, and Sentinel-2A data used in this study. We are also thankful for various data depositaries who made the global LAI products available (Table 2).

Appendix A. Field measured reflectance data over the Honghe area in 2013

Field reflectance data were obtained with an AvaField 3 spectroradiometer (Avantes, Apeldoorn, The Netherlands) over the Honghe area in June and July, respectively (Table A1). The field measurements were made between 9:00 AM and 12:00 AM local time, corresponding to the HJ-1 satellite overpasses on June 24 and July 15, 2013, respectively.

Table A1

HJ-1 and field measured red (630–690 nm) and near infrared (NIR, 760–900 nm) reflectance data over the Honghe area in 2013.

Date (YYYYMMDD)	Field type	Latitude (°)	Longitude (°)	Red		NIR	
				HJ-1	Field	HJ-1	Field
2013/06/22	Grass	47.5160	133.5774	0.1040	0.0588	0.3091	0.3031
2013/06/22	Rice	47.7571	133.5423	0.0834	0.0817	0.2057	0.2235
2013/06/22	Soybean	47.5166	133.5754	0.1362	0.0957	0.2424	0.2097
2013/06/23	Concrete	47.5855	133.5097	0.2158	0.2090	0.3182	0.3149
2013/06/23	Grass	47.7423	133.5267	0.0862	0.0985	0.3791	0.3369
2013/06/23	Soybean	47.7584	133.5427	0.1301	0.0979	0.2631	0.2287
2013/07/15	Concrete	47.5855	133.5097	0.2446	0.3042	0.3380	0.3091
2013/07/15	Grass	47.7423	133.5267	0.1216	0.1242	0.3465	0.3300
2013/07/15	Rice	47.7571	133.5423	0.0959	0.1113	0.3793	0.3246
2013/07/16	Soybean	47.5875	133.4992	0.1092	0.1028	0.3410	0.3002
2013/07/16	Soybean	47.7584	133.5427	0.1155	0.1025	0.3951	0.3838
2013/07/16	Wetland	47.5853	133.4989	0.1023	0.1481	0.3742	0.3423

Appendix B. High resolution reference LAI maps over the study area

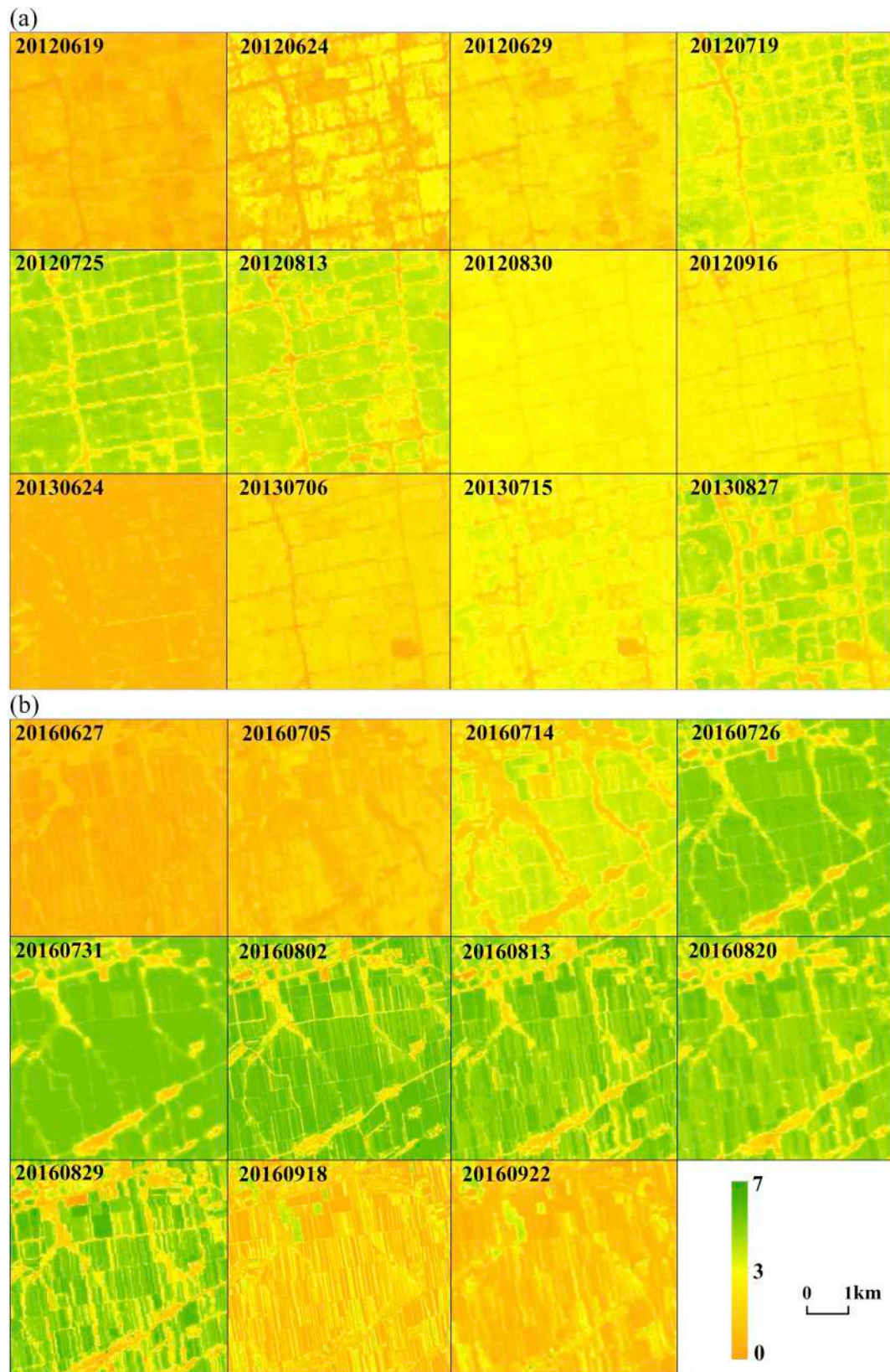


Fig. A1. High resolution reference LAI maps derived for Honghe (a) and Hailun (b). See [Table 4](#) for more information about the high resolution data.

Appendix C. Moderate resolution LAI products over the study area

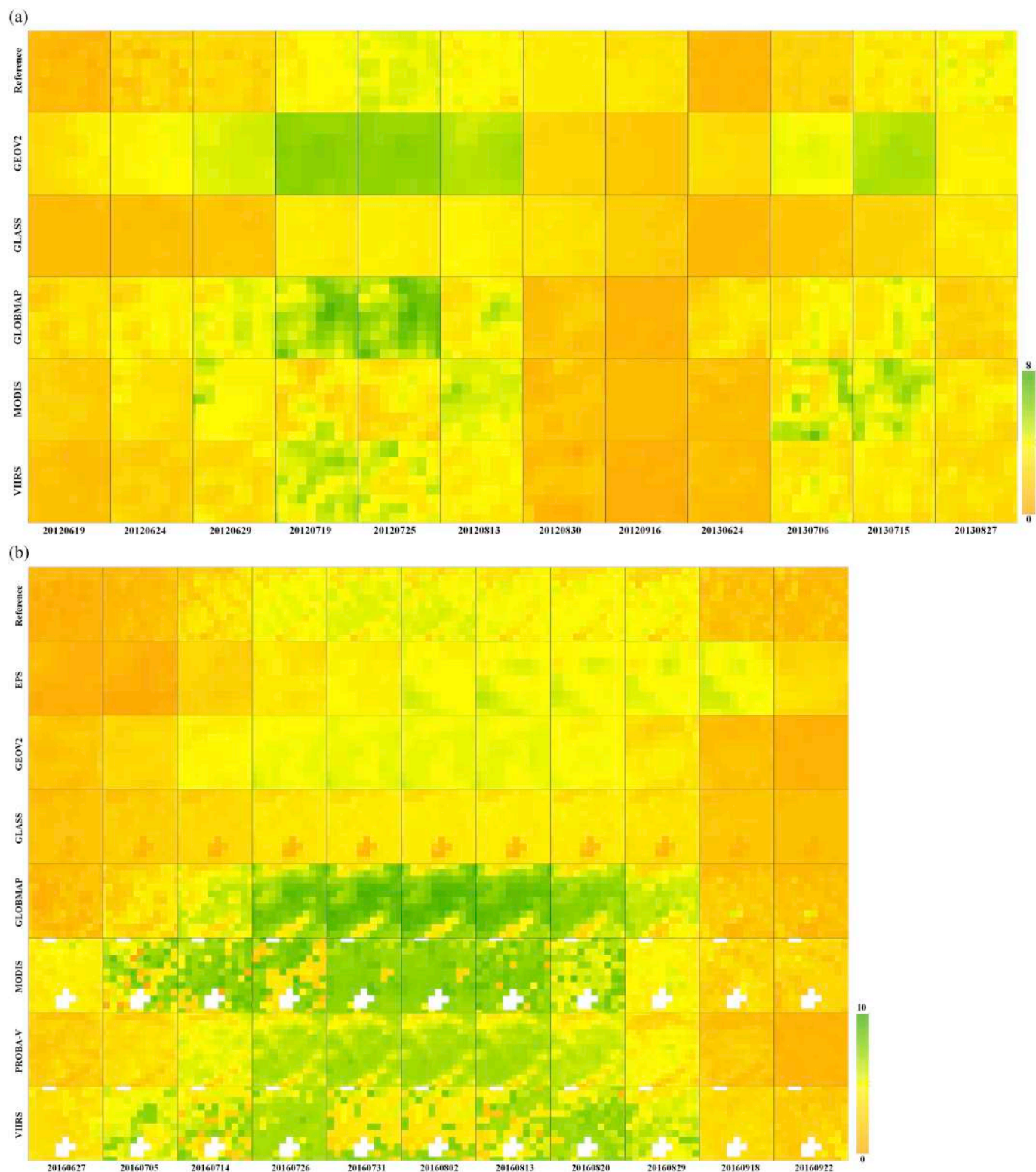


Fig. A2. Moderate resolution LAI products for EPS, GEOV2, GLASS, GLOBMAP, MODIS, PROBA-V, and VIIRS over Honghe in 2012 and 2013 (a) and Hailun in 2016 (b). The blank pixels in MODIS and VIIRS are build-up areas and have no valid data. The reference LAI (first row) is in 500 m and see Table 2 for the others. The date is shown at the bottom in YYYYMMDD (Table 4).

Appendix D. Supplementary data

Supplementary data associated with this article can be found in the online version, at doi:<https://doi.org/10.1016/j.rse.2019.111377>. These data

include the Google map of the most important areas described in this article.

References

- Ångström, A., 1961. Techniques of determining the turbidity of the atmosphere. *Tellus* 13, 214–223.
- Bacour, C., Jacquemoud, S., Tourbier, Y., Dechambre, M., Frangi, J.P., 2002. Design and analysis of numerical experiments to compare four canopy reflectance models. *Remote Sens. Environ.* 79, 72–83.
- Bai, D., Jiao, Z., Dong, Y., Zhang, X., Li, Y., He, D., 2017. Analysis of the sensitivity of the anisotropic flat index to vegetation parameters based on the two-layer canopy reflectance model. *Journal of Remote Sensing* 27, 1–11.
- Barbu, A.L., Calvet, J.C., Mahfouf, J.F., Lafont, S., 2014. Integrating ASCAT surface soil moisture and GEOV1 leaf area index into the SURFEX modelling platform: a land data assimilation application over France. *Hydrol. Earth Syst. Sci.* 18, 173–192.
- Baret, F., Morisette, J., Fernandes, R., Champeaux, J.L., Myneni, R., Chen, J., Plummer, S., Weiss, M., Bacour, C., Derive, G., 2006. Evaluation of the representativeness of networks of sites for the global validation and intercomparison of land biophysical products: proposition of the CEOS-BELMANIP. *IEEE Trans. Geosci. Remote Sens.* 44, 1794–1803.
- Baret, F., Hagolle, O., Geiger, B., Bicheron, P., Miras, B., Huc, M., Berthelot, B., Niño, F., Weiss, M., Samain, O., Roujean, J.L., Leroy, M., 2007. LAI, FPAR, and FCOVER CYCLOPES global products derived from VEGETATION part 1: principles of the algorithm. *Remote Sens. Environ.* 110, 275–286.
- Baret, F., Weiss, M., Lacaze, R., Camacho, F., Makhmara, H., Pacholczyk, P., Smets, B., 2013. GEOV1: LAI, FPAR essential climate variables and FCOVER global time series capitalizing over existing products. Part1: principles of development and production. *Remote Sens. Environ.* 137, 309–399.
- Baret, F., Weiss, M., Verger, A., Smets, B., 2016. ATBD for LAI, FPAR and FCOVER From PROBA-V Products at 300M Resolution (GEOV3). *IMAGINES_RP2.1_ATBD-LAI300M*. pp. 61. <http://fp7-imagines.eu/pages/documents.php>.
- Boisier, J.P., de Noblet-Ducoudré, N., Ciais, P., 2014. Historical land-use-induced evapotranspiration changes estimated from present-day observations and reconstructed land-cover maps. *Hydrol. Earth Syst. Sci.* 18, 3571–3590.
- Camacho, F., Cernicharo, J., Lacaze, R., Baret, F., Weiss, M., 2013. GEOV1: LAI, FPAR essential climate variables and FCOVER global time series capitalizing over existing products. Part 2: validation and intercomparison with reference products. *Remote Sens. Environ.* 137, 310–329.
- Campos-Taberner, M., García-Haro, F., Busetto, L., Ranghetti, L., Martínez, B., Gilabert, M.A., Camps-Valls, G., Camacho, F., Boschetti, M., 2018. A critical comparison of remote sensing leaf area index estimates over Rice-cultivated areas: from Sentinel-2 and Landsat-7/8 to MODIS, GEOV1 and EUMETSAT polar system. *Remote Sens.* 10, 763. <https://doi.org/10.3390/rs10050763>.
- Casa, R., Varella, H., Buis, S., Guérif, M., De Solan, B., Baret, F., 2012. Forcing a wheat crop model with LAI data to access agronomic variables: evaluation of the impact of model and LAI uncertainties and comparison with an empirical approach. *Eur. J. Agron.* 37, 1–10.
- Casanova, D., Epema, G.F., Goudriaan, J., 1998. Monitoring rice reflectance at field level for estimating biomass and LAI. *Field Crop Res.* 55, 83–92.
- Chen, J.M., Leblanc, S.G., 1997. A four-scale bidirectional reflectance model based on canopy architecture. *IEEE Trans. Geosci. Remote Sens.* 35, 1316–1337.
- Chen, J.M., Menges, C.H., Leblanc, S.G., 2005. Global mapping of foliage clumping index using multi-angular satellite data. *Remote Sens. Environ.* 97, 447–457.
- Chen, J.M., Deng, F., Chen, M., 2006. Locally adjusted cubic-spline capping for reconstructing seasonal trajectories of a satellite-derived surface parameter. *IEEE Trans. Geosci. Remote Sens.* 44, 2230–2238.
- Cheng, Q., 2008. Validation and correction of MODIS-LAI using in situ rice LAI in southern China. *Commun. Soil Sci. Plant Anal.* 39, 1658–1669.
- Claverie, M., Vermote, E.F., Weiss, M., Baret, F., Hagolle, O., Demarez, V., 2013. Validation of coarse spatial resolution LAI and FPAR time series over cropland in Southwest France. *Remote Sens. Environ.* 139, 216–230.
- Darvishzadeh, R., Skidmore, A., Schlerf, M., Atzberger, C., 2008. Inversion of a radiative transfer model for estimating vegetation LAI and chlorophyll in a heterogeneous grassland. *Remote Sens. Environ.* 112, 2592–2604.
- Deng, F., Chen, J.M., Plummer, S., Chen, M., Pisek, J., 2006. Algorithm for global leaf area index retrieval using satellite imagery. *IEEE Trans. Geosci. Remote Sens.* 44, 2219–2229.
- Duveiller, G., Weiss, M., Baret, F., Defourny, P., 2011. Retrieving wheat green area index during the growing season from optical time series measurements based on neural network radiative transfer inversion. *Remote Sens. Environ.* 115, 887–896.
- Fang, H., Wei, S., Liang, S., 2012. Validation of MODIS and CYCLOPES LAI products using global field measurement data. *Remote Sens. Environ.* 119, 43–54.
- Fang, H., Jiang, C., Li, W., Wei, S., Baret, F., Chen, J.M., García-Haro, J., Liang, S., Liu, R., Myneni, R.B., Pinty, B., Xiao, Z., Zhu, Z., 2013. Characterization and intercomparison of global moderate resolution leaf area index (LAI) products: analysis of climatologies and theoretical uncertainties. *J. Geophys. Res. Biogeosci.* 118, 529–548.
- Fang, H., Li, W., Wei, S., Jiang, C., 2014. Seasonal variation of leaf area index (LAI) over paddy rice fields in NE China: Intercomparison of destructive sampling, LAI-2200, digital hemispherical photography (DHP), and AccuPAR methods. *Agric. For. Meteorol.* 198–199, 126–141.
- Fang, H., Ye, Y., Liu, W., Wei, S., Ma, L., 2018. Continuous estimation of canopy leaf area index (LAI) and clumping index over broadleaf crop fields: an investigation of the PASTIS-57 instrument and smartphone applications. *Agric. For. Meteorol.* 253–254, 48–61.
- Fang, H., Baret, F., Plummer, S., Schaepman-Strub, G., 2019. An overview of global leaf area index (LAI): methods, products, validation, and applications. *Rev. Geophys.* <https://doi.org/10.1029/2018RG000608>.
- Feret, J.-B., François, C., Asner, G.P., Gitelson, A.A., Martin, R.E., Bidet, L.P.R., Ustin, S.L., le Maire, G., Jacquemoud, S., 2008. PROSPECT-4 and 5: advances in the leaf optical properties model separating photosynthetic pigments. *Remote Sens. Environ.* 112, 3030–3043.
- Fernandes, R., Plummer, S., Nightingale, J., Baret, F., Camacho, F., Fang, H., Garrigues, S., Gobron, N., Lang, M., Lacaze, R., LeBlanc, S., Meroni, M., Martínez, B., Nilsson, T., Pinty, B., Pisek, J., Sonnentag, O., Verger, A., Welles, J., Weiss, M., Widlowski, J.L., 2014. Global leaf area index product validation good practices. In: Schaepman-Strub, G., Román, M., Nickeson, J. (Eds.), *Best Practice for Satellite-Derived Land Product Validation*, pp. 78. <https://doi.org/10.5067/doc/ceoswgc/1pv/lai.002>.
- García-Haro, F.J., Campos-Taberner, M., Muñoz-Marí, J., Laparra, V., Camacho, F., Sánchez-Zapero, J., Camps-Valls, G., 2018. Derivation of global vegetation biophysical parameters from EUMETSAT polar system. *ISPRS J. Photogramm. Remote Sens.* 139, 57–74.
- Garrigues, S., Lacaze, R., Baret, F., Morisette, J.T., Weiss, M., Nickeson, J.E., Fernandes, R., Plummer, S., Shabanov, N.V., Myneni, R.B., Knyazikhin, Y., Yang, W., 2008a. Validation and intercomparison of global leaf area index products derived from remote sensing data. *J. Geophys. Res.* 113, G02028. <https://doi.org/10.1029/2007JG000635>.
- Garrigues, S., Shabanov, N., Swanson, K., Morisette, J.T., Baret, F., Myneni, R., 2008b. Intercomparison and sensitivity analysis of leaf area index retrievals from LAI-2000, AccuPAR, and digital hemispherical photography over croplands. *Agric. For. Meteorol.* 148, 1193–1209.
- Gastellu-Etchegorry, J.-P., Yin, T., Lauret, N., Cajgfinger, T., Gregoire, T., Grau, E., Feret, J.-B., Lopes, M., Guilleux, J., Dedieu, G., Malenkovský, Z., Cook, B., Morton, D., Rubio, J., Durrieu, S., Cazanave, G., Martin, E., Ristorcelli, T., 2015. Discrete anisotropic radiative transfer (DART 5) for modeling airborne and satellite Spectroradiometer and LIDAR acquisitions of natural and urban landscapes. *Remote Sens.* 7, 1667–1701.
- GCOS, 2011. Systematic Observation Requirements for Satellite-based Products for Climate, 2011 Update, Supplemental Details to the Satellite-based Component of the Implementation Plan for the Global Observing System for Climate in Support of the UNFCCC (2010 Update). GCOS-154. pp. 138. https://library.wmo.int/doc_num.php?explnum_id=3710.
- GCOS, 2016. The Global Observing System for Climate: Implementation Needs (GCOS-200). World Meteorological Organization. https://library.wmo.int/doc_num.php?explnum_id=3417.
- Gessner, U., Niklaus, M., Kuenzer, C., Dech, S., 2013. Intercomparison of leaf area index products for a gradient of sub-humid to arid environments in West Africa. *Remote Sens.* 5, 1235–1257.
- Groenendijk, M., Dolman, A.J., Ammann, C., Arneth, A., Cescatti, A., Dragoni, D., Gash, J.H.C., Gianelle, D., Gioli, B., Kiely, G., Knohl, A., Law, B.E., Lund, M., Marcolla, B., van der Molen, M.K., Montagnani, L., Moors, E., Richardson, A.D., Rouspard, O., Verbeeck, H., Wohlfahrt, G., 2011. Seasonal variation of photosynthetic model parameters and leaf area index from global Fluxnet eddy covariance data. *J. Geophys. Res.* 116, G04027. <https://doi.org/10.1029/2011jg001742>.
- Haboudane, D., Miller, J.R., Pattey, E., Zarco-Tejada, P.J., Strachan, I.B., 2004. Hyperspectral vegetation indices and novel algorithms for predicting green LAI of crop canopies: modeling and validation in the context of precision agriculture. *Remote Sens. Environ.* 90, 337–352.
- He, L., Chen, J.M., Pisek, J., Schaaf, C.B., Strahler, A.H., 2012. Global clumping index map derived from the MODIS BRDF product. *Remote Sens. Environ.* 119, 118–130.
- Houberg, R., Soegaard, H., Boegh, E., 2007. Combining vegetation index and model inversion methods for the extraction of key vegetation biophysical parameters using Terra and Aqua MODIS reflectance data. *Remote Sens. Environ.* 106, 39–58.
- Huang, D., Knyazikhin, Y., Wang, W., Deering, D.W., Stenberg, P., Shabanov, N., Tan, B., Myneni, R.B., 2008. Stochastic transport theory for investigating the three-dimensional canopy structure from space measurements. *Remote Sens. Environ.* 112, 35–50.
- Jégo, G., Pattey, E., Liu, J., 2012. Using leaf area index, retrieved from optical imagery, in the STICS crop model for predicting yield and biomass of field crops. *Field Crop Res.* 131, 63–74.
- Jiang, Z., Chen, Z., Ren, J., 2011. The inversion of vegetation leaf area index based on the canopy radiative transfer model ACRM. *Chinese Journal of Agricultural Resources and Regional Planning* 32, 57–73.
- Jiang, C., Fang, H., 2019. GSV: a general model for hyperspectral soil reflectance simulation. *International Journal of Applied Earth Observation and Geoinformation* 83, 101932. <https://doi.org/10.1016/j.jag.2019.101932>.
- Kimura, R., Kamichika, M., Okada, S., Miura, H., 2004. Relationships among the leaf area index, moisture availability, and spectral reflectance in an upland rice field. *Agric. Water Manag.* 69, 83–100.
- Knyazikhin, Y., Martonchik, J.V., Diner, D.J., Myneni, R.B., Verstraete, M., Pinty, B., Gobron, N., 1998a. Estimation of vegetation canopy leaf area index and fraction of absorbed photosynthetically active radiation from MISR data. *J. Geophys. Res.* 103 (32), 239–232, 256.
- Knyazikhin, Y., Martonchik, J.V., Myneni, R.B., Dine, D.J., Running, S.W., 1998b. Synergistic algorithm for estimating vegetation canopy leaf area index and fraction of absorbed photosynthetically active radiation from MODIS and MISR data. *J. Geophys. Res.* 103 (32), 232–257 (276).

- Kotchenova, S.Y., Vermote, E.F., Matarrese, R., Klemm, J., Frank, J., 2006. Validation of a vector version of the 6S radiative transfer code for atmospheric correction of satellite data. Part I: path radiance. *Appl. Opt.* 45, 6762–6774.
- Kuusk, A., 2001. A two-layer canopy reflectance model. *J. Quant. Spectrosc. Radiat. Transf.* 71, 1–9.
- Lafont, S., Zhao, Y., Calvet, J.C., Peylin, P., Ciais, P., Maignan, F., Weiss, M., 2012. Modelling LAI, surface water and carbon fluxes at high-resolution over France: comparison of ISBA-A-gs and ORCHIDEE. *Biogeosciences* 9, 439–456.
- Levy, R., Hsu, C., et al., 2015. MODIS Atmosphere L2 Aerosol Product. NASA MODIS Adaptive Processing System, Goddard Space Flight Center, USA. <https://doi.org/10.5067/MODIS/MOD04.L2.006>.
- Li, W., Fang, H., 2015. Estimation of direct, diffuse, and total FPARs from Landsat surface reflectance data and ground-based estimates over six FLUXNET sites. *Journal of Geophysical Research-Biogeosciences* 120, 96–112.
- Li, Y., Ni, S., Wang, X., Wang, J., 2003. Simulating nadir reflectance of rice canopy. *Acta Agron. Sin.* 29, 397–401.
- Liu, R., Liu, Y., 2013. Generation of new cloud masks from MODIS land surface reflectance products. *Remote Sens. Environ.* 133, 21–37.
- Liu, Y., Liu, R., Chen, J.M., 2012. Retrospective retrieval of long-term consistent global leaf area index (1981–2011) from combined AVHRR and MODIS data. *J. Geophys. Res. Biogeosci.* 117, G04003. <https://doi.org/10.1029/2012JG002084>.
- Liu, J., Patteny, E., Admiral, S., 2013. Assessment of in situ crop LAI measurement using unidirectional view digital photography. *Agric. For. Meteorol.* 169, 25–34.
- Morisette, J.T., Baret, F., Privette, J.L., Myneni, R.B., Nickeson, J.E., Garrigues, S., Shabanov, N.V., Weiss, M., Fernandes, R.A., Leblanc, S.G., Kalacska, M., Sanchez-Azofeifa, G.A., Chubey, M., Rivard, B., Stenberg, P., Rautiainen, M., Voipio, P., Manninen, T., Pilant, A.N., Lewis, T.E., Hames, J.S., Colombo, R., Meroni, M., Busetto, L., Cohen, W.B., Turner, D.P., Warner, E.D., Petersen, G.W., Seufert, G., Cook, R., 2006. Validation of global moderate-resolution LAI products: a framework proposed within the CEOS land product validation subgroup. *IEEE Trans. Geosci. Remote Sens.* 44, 1804–1817.
- Müller-Wilm, U., 2018. Sen2Cor Configuration and User Manual. Telespazio VEGA Deutschland GmbH, Darmstadt, Germany Ref. S2-PDGS-MPC-L2ASUM-V2.5.5. <http://step.esa.int/thirdparties/sen2cor/2.5.5/docs/S2-PDGS-MPC-L2A-SUM-V2.5.5.V2.pdf>.
- Myneni, R.B., Ramakrishna, R., Nemani, R., Running, S.W., 1997. Estimation of global leaf area index and absorbed par using radiative transfer models. *IEEE Transactions on Geosciences and Remote Sensing* 35, 1380–1393.
- Myneni, R.B., Hoffman, S., Knyazikhin, Y., Privette, J.L., Glassy, J., Tian, Y., Wang, Y., Song, X., Zhang, Y., Smith, G.R., Lotsch, A., Friedl, M., Morisette, J.T., Votava, P., Nemani, R.R., Running, S.W., 2002. Global products of vegetation leaf area and fraction absorbed PAR from year one of MODIS data. *Remote Sens. Environ.* 83, 214–231.
- Myneni, R., Knyazikhin, Y., Park, T., 2015. MCD15A2H MODIS/Terra + Aqua Leaf Area Index/FPAR 8-Day L4 Global 500m SIN Grid V006 [Data Set]. NASA EOSDIS Land Processes DAAC <https://doi.org/10.5067/MODIS/MCD15A2H.006>.
- Ogutu, B., Dash, J., Dawson, T.P., 2011. Evaluation of leaf area index estimated from medium spatial resolution remote sensing data in a broadleaf deciduous forest in southern England, UK. *Can. J. Remote. Sens.* 37, 333–347.
- Richter, K., Atzberger, C., Vuolo, F., D'Urso, G., 2011. Evaluation of Sentinel-2 spectral sampling for radiative transfer model based LAI estimation of wheat, sugar beet, and maize. *IEEE Journal of Selected Topics in Applied Earth Observations and Remote Sensing* 4, 458–464.
- Shibayama, M., Akiyama, T., 1989. Seasonal visible, near-infrared and mid-infrared spectra of rice canopies in relation to LAI and above-ground dry phytomass. *Remote Sens. Environ.* 27, 119–127.
- Shibayama, M., Sakamoto, T., Takada, E., Inoue, A., Morita, K., Takahashi, W., Kimura, A., 2011. Estimating Paddy Rice leaf area index with fixed point continuous observation of near infrared reflectance using a calibrated digital camera. *Plant Production Science* 14, 30–46.
- Stern, A.J., Doraiswamy, P.C., Hunt, E.R., 2014. Comparison of different MODIS data product collections over an agricultural area. *Remote Sensing Letters* 5 (1), 1–9.
- Sun, T., Fang, H., Liu, W., Ye, Y., 2017. Impact of water background on canopy reflectance anisotropy of a paddy rice field from multi-angle measurements. *Agric. For. Meteorol.* 233, 143–152.
- Tang, H., Yu, K., Hagolle, O., Jiang, K., Geng, X., Zhao, Y., 2013. A cloud detection method based on a time series of MODIS surface reflectance images. *International Journal of Digital Earth* 6, 157–171.
- Urrutia, J.A.S., 2010. Validation of the Leaf Area Index Product from MODIS-15 for Rice Using a Soil-Leaf-Canopy Radiative Transfer Model a Case Study of Seville, Spain. M.Sc Thesis. Geo-Information Science and Earth Observation for Environmental Modelling and Management: University of Twente, pp. 53.
- Vaesens, K., Gilliams, S., Nackaerts, K., Coppin, P., 2001. Ground-measured spectral signatures as indicators of ground cover and leaf area index: the case of paddy rice. *Field Crop Res.* 69, 13–25.
- Verger, A., Baret, F., Weiss, M., 2014a. Near real-time vegetation monitoring at global scale. *Selected Topics in Applied Earth Observations and Remote Sensing, IEEE Journal of* 7, 3473–3481.
- Verger, A., Baret, F., Weiss, M., Smets, B., Camacho, F., Lacaze, R., 2014b. GEOV2: Near real time estimation of LAI, FAPAR and cover fraction variables from VEGETATION data within Copernicus global land service. In: Sobrino, J.A. (Ed.), *The 4th International Symposium on Recent Advances in Quantitative Remote Sensing*, pp. 467–471 (Torrent, Spain).
- Verhoef, W., Bach, H., 2007. Coupled soil-leaf-canopy and atmosphere radiative transfer modeling to simulate hyperspectral multi-angular surface reflectance and TOA radiance data. *Remote Sens. Environ.* 109, 166–182.
- Vermote, E., 2015. MOD09A1 MODIS/Terra Surface Reflectance 8-Day L3 Global 500m SIN Grid V006 [Data Set]. NASA EOSDIS LP DAAC <https://doi.org/10.5067/MODIS/MOD09A1.006>.
- Vermote, E., Tanré, D., Deuze, J.L., Herman, M., Morcrette, J.J., 1997. Second simulation of the satellite signal in the solar spectrum, 6S-an overview. *IEEE Trans. Geosci. Remote Sens.* 35, 675–686.
- Vermote, E., Justice, C., Claverie, M., Franch, B., 2016. Preliminary analysis of the performance of the Landsat 8/OLI land surface reflectance product. *Remote Sens. Environ.* 185, 46–56.
- Weiss, M., Baret, F., Garrigues, S., Lacaze, R., 2007. LAI and fPAR CYCLOPES global products derived from VEGETATION. Part 2: validation and comparison with MODIS collection 4 products. *Remote Sens. Environ.* 110, 317–331.
- Widlowski, J.-L., 2015. Conformity testing of satellite-derived quantitative surface variables. *Environ. Sci. Pol.* 51, 149–169.
- Wu, X., Cheng, Q., Mao, Z., 2006. Validation of MOD15-LAI and MOD13 using in situ rice data. In: Kuligowski, R.J., Parihar, J.S., Saito, G. (Eds.), *Agriculture and Hydrology Applications of Remote Sensing*, <https://doi.org/10.1117/12.693314>. (64111F-64111F-64111F-64119).
- Xiao, X., Boles, S., Froking, S., Li, C., Babu, J.Y., Salas, W., Moore, Iii, B., 2006. Mapping paddy rice agriculture in south and Southeast Asia using multi-temporal MODIS images. *Remote Sens. Environ.* 100, 95–113.
- Xiao, Z., Liang, S., Wang, J., Chen, P., Yin, X., Zhang, L., Song, J., 2014. Use of general regression neural networks for generating the GLASS leaf area index product from time-series MODIS surface reflectance. *IEEE Trans. Geosci. Remote Sens.* 52, 209–223.
- Yan, K., Park, T., Yan, G., Chen, C., Yang, B., Liu, Z., Nemani, R., Knyazikhin, Y., Myneni, R., 2016a. Evaluation of MODIS LAI/FPAR product collection 6. Part 1: consistency and improvements. *Remote Sens.* 8, 359. <https://doi.org/10.3390/rs8050359>.
- Yan, K., Park, T., Yan, G., Liu, Z., Yang, B., Chen, C., Nemani, R., Knyazikhin, Y., Myneni, R., 2016b. Evaluation of MODIS LAI/FPAR product collection 6. Part 2: validation and intercomparison. *Remote Sens.* 8, 460. <https://doi.org/10.3390/rs8060460>.
- Yan, K., Park, T., Chen, C., Xu, B., Song, W., Yang, B., Zeng, Y., Liu, Z., Yan, G., Knyazikhin, Y., Myneni, R.B., 2018. Generating global products of LAI and FPAR from SNPP-VIIRS data: theoretical background and implementation. *IEEE Trans. Geosci. Remote Sens.* 56, 2119–2137.